Re-equilibration history and P–T path of eclogites from Variscan Sardinia, Italy: a case study from the medium-grade metamorphic complex

G. Cruciani; · M. Franceschelli;C. Groppo; · G. Oggiano; ·M.E. Spano. Re■equilibration history and P–T path of eclogites from VariscanSardinia, Italy: a case study from the medium■grademetamorphic complex. INTERNATIONAL JOURNAL OF EARTH SCIENCES. 104 (-) pp: 797-814.
DOI: 10.1007/s00531-014-1095-5

Re-equilibration history and P-T path of eclogites from Variscan Sardinia, Italy: a case study from the medium-grade metamorphic Complex

Gabriele Cruciani[1], Marcello Franceschelli[1*], Chiara Groppo [2], Giacomo Oggiano[3], Maria Elena Spano[1]

1 Dipartimento Scienze Chimiche e Geologiche, Università di Cagliari.

2 Dipartimento di Scienze della Terra, Università di Torino

3 Dipartimento di Scienze Botaniche, Ecologiche e Geologiche, Università di Sassari

*Corresponding author

Prof. Marcello Franceschelli,

Dipartimento Scienze Chimiche e Geologiche, Università di Cagliari

Tel. +39 070 6757713, Fax. +39 070 282236

E-mail address: francmar@unica.it

Abstract Retrogressed eclogites are hosted within the Variscan Low- to Medium-Grade Metamorphic Complex near Giuncana, north-central Sardinia. These rocks are medium- to fine-grained with garnet and amphibole as the most abundant mineral phases along with clinopyroxene, plagioclase, quartz, biotite, chlorite, epidote, ilmenite, rutile and titanite. Four stages of mineralogical re-equilibration have been distinguished. The stage I is characterized by the occurrence of omphacite, epidote, quartz, amphibole, rutile and ilmenite in garnet poikiloblasts. The stage II is characterized by two types of symplectitic microstructures: (i) amphibole + quartz symplectite, and (ii) clinopyroxene + plagioclase ± amphibole symplectite. The first symplectite type replaces omphacite included in garnet, whereas the second one is widespread in the matrix. Biotite droplets and/or lamellae intimately growing with fine-grained plagioclase resemble biotite + plagioclase symplectite after phengite. The stage III is characterized by the widespread formation of amphibole: (i) as zoned porphyroblasts in the matrix, (ii) as corona-type microstructure replacing garnet. Subordinate plagioclase (oligoclase) is also present in the amphibole corona. The stage IV is characterized by the local formation of biotite replacing garnet, actinolite, chlorite, albite and titanite. P-T pseudosections calculated with Perple_X give P-T conditions $580<T<640$°C, $1.3<P<1.8$ GPa for the stage I. After the stage I, pressure decrease and temperature increase led to the breakdown of omphacite with the formation of clinopyroxene + plagioclase ± amphibole symplectite at ~1.30-1.45 GPa and 660-730°C (stage II). P-T conditions of the amphibolite-facies stage III have been defined at 600-670°C, P=0.65-0.95 GPa. P-T conditions of the latest stage IV are in the range of greenschist-facies. The P-T path of the retrogressed eclogite hosted in the medium-grade micaschist and paragneiss of Giuncana recalls the P-T trajectory of retrogressed eclogite hosted in the migmatite Complex of northern Sardinia. The eclogites from Giuncana do not preserve the prograde segment of the P-T path but, similarly to the other Sardinian eclogites, they record a slight increase in temperature during exhumation. This suggest that the thermal flow responsible for the amphibolitic-granulitic event post-dating the eclogitic stage recorded in the

Giuncana eclogite may be tentatively referred to the slab break-off also responsible for the production of Mg-K suite in Corsica.

Keywords*:* retrogressed eclogite; Nappe Zone; mineralogical re-equilibration; P-T path; northern Sardinia; Variscan Orogeny

Introduction

The southern Variscan branch shows a complex collisional frame, characterized by changes in kinematics, which during the late collisional stage assumed a broad transpressive character (Carosi and Oggiano 2002; Denele et al. 2007; Gebelin et al. 2009; Martinez Catalan 2011). From the Central Iberia Massif through the French Massif Central and Western Alps to Bohemian Massif, the Variscides host many alloctonous units characterized by Siluro-Devonian HP and/or UHP assemblages, which is expected in connection with oceanic sutures. These should be related to the closure of oceanic seaways between Gondwana and the ribbon of terranes interposed between this supercontinent and Laurussia. However the association of the crustal nappes hosting HP ophiolites with oceanic sutures inside the Variscides is still debated (Iberian- Czech Belt: Keppie et al. 2010), and also the existence of oceanic domains between Gondwana and Armorica (or ATA, or Hun superterrane) has been questioned on palaeogeographic base (e.g. Robardet 2003).

The geological features of the Sardinia Variscides partially match those of different sectors of the Southern Variscan Realm for the presence of: (i) a foreland of Gondwanan affinity; (ii) a stack of low grade tectonic units, bearing Cambro-Ordovician volcanic and sedimentary successions transported on the foreland, and (iii) an inner zone, located to the north of the island and in Corsica (Carmignani et al. 1994; Rossi et al. 2009).

The inner zone contains a high grade (High Grade Metamorphic Complex: HGMC) and a low-medium grade metamorphic unit (Low- to Medium-Grade Metamorphic Complex: L-MGMC), which are juxtaposed to the low grade nappe stack. The inner zone shares meaningful features with

the allochtonous units with ophiolites and HP rocks of the Massif Central (Lardeaux et al. 2001), as well as with the Gföhl Unit and Monotonous and Varied units of the Moldanubian Zone (Faryad et al. 2013 and bibliography therein)

In this paper we present new data on the Sardinian retrogressed eclogites embedded in the L-MGMC and we compare these eclogites with those of the HGMC, with the aim of improving the knowledge of the petrogenesis and P-T paths of Sardinian eclogites. The metabasite with eclogite facies relics enclosed in the HGMC experienced a P-T evolution characterized by a temperature increase during exhumation from the eclogitic stage to the granulitic stage (Cruciani et al. 2011, 2012; Franceschelli et al. 2005, 2007): this P-T evolution is slightly different from the P-T history recorded by other Variscan eclogites (e.g. in central Europe), prevalently characterized by isothermal decompression (O'Brien 2000). Confirming whether or not such heating during decompression is recorded also by the L-MGMC metabasite with eclogite facies relics is therefore important for a better understanding of the early stages of Variscan orogenesis in Sardinia. The results are discussed in the general framework of the Variscan Europe, and contribute to the reconstruction of the Variscan puzzle in the northern Gondwana margin.

Geological framework of the study area

In the Variscan segment of the Corsica-Sardinia microplate, the metamorphic grade increases from anchimetamorphism (Eltrudis et al. 1995) in southern Sardinia, to the garnet-zone (Franceschelli et al. 1990) and to the sillimanite + K-feldspar zone (Ricci et al. 2004) with migmatite (Cruciani et al. 2008a,b) and granulite (Franceschelli et al. 2002; Giacomini et al. 2008) in the Inner Zone of northern Sardinia and its extension on Corsica.

The inner zone is characterized by a high grade metamorphic complex (HGMC) juxtaposed on a medium grade metamorphic unit (L-MGMC). These two complexes are believed to be deeply rooted in a suture zone (Capelli et al. 1992, Rossi et al. 2009), based on the occurrence of more or less retrogressed eclogite. The HGMC mostly consists of anatectic orthogneisses and metapelites

and hosts metabasite bodies, kilometer to meter sized, which experienced an early eclogitic stage overprinted by an intermediate-HP granulitic event with temperature exceeding 800 °C and pressure in the range of 1.3 GPa (Cortesogno et al. 2004; Cruciani et al. 2012; Franceschelli et al. 2007; Giacomini et al. 2005a). The L-MGMC largely outcropping adjacent to the southern side of the Posada-Asinara Line, consists of both igneous and sedimentary sequences (orthogneiss, micaschist, paragneiss and rare marble and amphibolite lenses). The contact between the L-MGMC and the HGMC locally consists (e.g. Asinara island: Cappelli et al. 1992) of a top-to-the-southwest thrust; elsewhere it results in a retrogressive dextral strike-slip shear zone (e.g. Posada valley: Elter et al. 1990) and it is known as Posada-Asinara Line (PAL).

The study area in north Sardinia is located in the L-MGMC, close to the contact with the HGMC. Here the contact between the L-MGMC and the HGMC is represented by a ductile dextral strike-slip shear zone with reverse component (Carosi et al. 2012; Casini et al. 2010). This shear zone results in a 200 m thick phyllonite belt sandwiched between Grt + St + Ky- bearing micaschists and paragneisses, and mylonitic migmatites derived from the HGMC. P-T estimates in the micaschists are in the range 580-635 °C and 0.7-0.9 GPa; the retrogressive shear zone equilibrated under upper greenschist-facies conditions (Casini et al. 2010). Up to now there is no geochronological evidence for the age of high-pressure metamorphism of Giuncana eclogite; only the age of protolith (454 ± 6 Ma) is known (Cruciani et al. 2013b). The age of the Barrovian metamorphism is dated at 350 Ma (Carosi et al. 2012; Del Moro et al. 1991). The shear zone exhibits evidence of a complex deformative history; according to Frassi et al. (2009), relict kinematic indicators could suggest a pristine sinistral motion that switched into dextral during the retrogressive evolution. The deformative history of the L-MGMC that hosts the eclogite, can be described in terms of three folding phases (Frassi et al. 2009). The D_1 phase is barely testified by inclusion trails of S_1 relic foliation in garnet and oligoclase. D_2 is coeval with respect to the growth of garnet, oligoclase, staurolite and kyanite porphyroblasts. In fact the inclusion trails in these blastic phases are at high angle, but continuous, with the external foliation S_2. D_2 hinges are hardly preserved and generally

show steeply plunging axis; moving toward the phyllonite they tend to be decrenulated and S_2 merges with the mylonitic foliation, here named S_4. A late folding phase generates open folds with steep axial planes. These folds have sub-horizontal axis trending N130, that is at an angle of 20-30° with the shear zone. No meaningful blastesis and only a spaced crenulation cleavage are associated to this late folding phase.

The eclogitic bodies are embedded within micaschists and paragneisses which recorded pervasive non coaxial deformation linked to the development of S_2 foliation. Some meter-sized blocks result completely equilibrated under amphibolite-facies conditions. The larger eclogite body is hectometric in size, has sub-rounded shape and crops out one km SW of the phyllonite belt (Fig. 1). The greenschist-facies retrogressive imprint on the hosting paragneisses is weak and the Grt + Olig + St + Ky assemblage is well preserved. The relics of the eclogitic assemblage and texture are still evident in the core of the wider eclogite body, whereas the re-equilibration into amphibolite-facies assemblage is restricted to the contact with the host micaschists. The inner part of the eclogite body is poorly deformed; only the amphiboles of the outer part, close to the contact with the host micaschists, exhibit a weak shape preferred orientation consistent with the D_2 deformative phase. This suggests that D_2 controlled the uplift and emplacement of the eclogite at a depth compatible with the host intermediate-pressure micaschists.

Petrography

Two main types of metabasite occur in the Giuncana area: amphibolites and retrogressed eclogites. The amphibolite represents the dominant lithology and derives from a pervasive re-equilibration of the eclogite. The amphibolite consists of plagioclase and amphibole, ± garnet and epidote. No relics of omphacite or symplectitic microstructures were found. The retrogressed eclogite is a massive, medium- to fine-grained rock with abundant reddish garnet and green amphibole (Fig. 2a). They also contain variable amounts of clinopyroxene, plagioclase, quartz, biotite, chlorite, epidote, ilmenite, rutile, and titanite (Figs. 2b,c,d). Accessory minerals are apatite and zircon.

Millimetric garnet may be divided in two domains (Fig. 2b,c): a core domain with small inclusions of omphacite (Cpx_1), amphibole (Am_1), epidote (Ep_1), quartz, rutile, ilmenite and minor plagioclase (Pl_1), sometimes defining an internal faint foliation, and a rim domain which is free of inclusions or contains only few inclusions among those encountered in the core domain. Omphacite inclusions in garnet (Fig. 2c,d) are usually few tens to several tens of μm in size and have a rounded to irregular shape. They are often partially replaced at their rim by a amphibole (Am_{2a}) + quartz symplectite (Fig. 2d) or by a clinopyroxene + plagioclase ± amphibole (Am_{2b}) symplectitic assemblage (Fig. 3a). Although omphacite is widely preserved as armoured relics in garnet, it has never been observed in the rock matrix. Epidote (Ep_1) inclusions in garnet are often associated to plagioclase (Pl_1) (Fig. 2c). In few cases, epidote included in garnet is idioblastic. Two main types of epidote, similar for the microstructural position but different in composition, have been observed in garnet crystals: Fe-poor and Fe-rich epidote. Garnet also includes euhedral to subhedral amphibole crystals (Am_1) up to 50–70 μm in size, and anhedral quartz inclusions (Fig. 2c) with variable dimensions ranging from a few μm to a few tens of μm in size. Plagioclase (Pl_1) has never been observed as isolated inclusion, being always associated to epidote (Ep_1) in polymineralic inclusions.

Garnet poikiloblasts are set in a matrix mainly consisting of fine-grained clinopyroxene (Cpx_2) + plagioclase (Pl_{2a}) ± amphibole (Am_{2b}) symplectite (Fig. 2b). This symplectite ($Cpx_2 + Pl_{2a} \pm Am_{2b}$) is the most common in the studied rocks, and also replaces omphacite inclusions in garnet (Fig. 3a). It forms patches up to a few millimeters in size (Fig. 2b) and consists of vermicular lamellae of clinopyroxene (Cpx_2) and plagioclase (Pl_{2a}), locally associated to subordinate (less than 10 vol.%) amphibole (Am_{2b}). The size, shape and orientation of the symplectite lamellae vary from one micro-domain to the other. Worth of note is the occurrence in the rock matrix of brownish biotite droplets (Bt_1) and/or lamellae intimately growing with fine-grained plagioclase (Pl_{2b}) (Fig. 3b). These microstructures resemble the biotite + plagioclase symplectites after phengite described by Groppo et al. (2007a) in the granulitized eclogites from the Ama Drime range of Eastern Himalayas. However, no relict phengite has been found in the investigated samples.

Garnet poikiloblasts are usually surrounded by a green amphibole rim (Fig. 3c) and, more rarely, by a poorly-developed, discontinuous corona of amphibole with subordinate plagioclase (Pl_3). The thickness of the amphibole coronas ranges from a few tens of μm up to a maximum of about 100 μm. These corona-type microstructures are less developed than those observed in other retrogressed eclogites from Sardinia (e.g. Cruciani et al. 2012; Franceschelli et al. 2007). Amphibole also occurs as zoned crystals (Am_3) growing pervasively in the rock matrix at the expense of the $Cpx_2 + Pl_{2a} \pm Am_{2b}$ symplectites (Fig. 3e). Matrix amphibole often shows a pale-green core rich in rutile needles oriented parallel to the amphibole cleavages (Fig. 3f). Rutile needles are most probably exsolved from an original Ti-rich amphibole. The rutile-rich core is mantled by a rutile-free green rim (Fig. 3f). Retrograde biotite (Bt_2) growing as small flakes in the matrix or replacing garnet and amphibole crystals has also been observed. In turn, biotite is partially replaced by chlorite and titanite. Anhedral and elongated epidote crystals (Ep_2) have also been observed in the rock matrix. Ilmenite is locally rimmed by titanite.

Mineral Chemistry

The chemical composition of minerals in the retrogressed eclogites was determined with a fully automated JEOL 8200 Super Probe at the Dipartimento di Scienze della Terra, University of Milano. Operating conditions were 15 kV accelerating voltage, beam current of 15 nA and 5–10 μm variable spot size. Natural and synthetic wollastonite, olivine, corundum, magnetite, rutile, orthoclase, jadeite, pure Mn, pure Cr, fluoro-phlogopite and barite were used as standards. Microstructural study, BSE imaging and additional EDS analyses were performed with a FEI Quanta 200 SEM equipped with an EDAX-EDS detector at the Centro Grandi Strumenti of Cagliari University. Selected microprobe analyses of garnet, amphibole, plagioclase, pyroxene, and biotite are reported in Table 1. Structural formulae have been calculated on the basis of 12, 8, and 6 oxygen for garnet, plagioclase and pyroxene, respectively. Amphibole structural formula has been

212 calculated using the Amph-IMA Program (Mogessie et al. 2004) with 23 oxygens and
213 normalization scheme.
214 *Garnet* - Garnet is almandine-rich (57-61 mol%) and spessartine-poor (1-3 mol%) with intermediate
215 grossularite and pyrope contents ranging from 24 to 30 mol% and 10 to 16 mol%, respectively.
216 Compositional traverses and X-ray maps show that garnet poikiloblasts are chemically
217 homogeneous or poorly zoned. In a poorly zoned garnet crystal from sample FC9 (Fig. 4a,b), X-
218 Ray mapping reveals a slight decrease in grossularite component counterbalanced by an increase in
219 pyrope from core to rim. However, the pyrope-rich and grossularite-poor rim domain is restricted to
220 the very outermost rim of garnet (≤ 10 μm). Almandine and spessartine contents are almost constant
221 from core to rim.
222 *Pyroxenes* - Na-Ca clinopyroxene inclusions in garnet (Cpx_1) are omphacite (Fig. 5a) with X_{Na} in
223 the range 0.4-0.5 and X_{Mg} in the range 0.60-0.76 [X_{Na} = Na/(Na+Ca); X_{Mg}= Mg/(Mg+Fe^{2+})]. No
224 compositional differences have been observed between omphacite partially replaced by the
225 amphibole + quartz symplectite and omphacite partially replaced by the clinopyroxene +
226 plagioclase ± amphibole symplectite. Clinopyroxene from the symplectite (Cpx_2) is diopside (Fig.
227 5b) with X_{Na} = 0.05-0.14, and X_{Mg} = 0.67-0.80.
228 *Amphiboles* - Amphiboles in different microstructural positions have different mineral chemistries
229 (Fig. 6a,b). All textural varieties are calcic amphiboles according to the classification of Leake et al.
230 (1997). Amphibole inclusions in garnet (Am_1) are Fe- pargasite/Al-Fe pargasite with X_{Mg}~0.46,
231 TiO_2 =0.7-1.2 wt% and Na_2O ~ 2 wt% or Mg-hornblende with higher X_{Mg} (0.64-0.68), lower TiO_2
232 (0.3-0.6 wt%) and lower Na_2O (1.1-1.5wt%).
233 Amphibole (Am_{2a}) from the Am + Qtz symplectite is Mg-hornblende to tschermakite with low TiO_2
234 (0.2-0.8 wt%) and Na_2O (~1 wt%) and X_{Mg} ~0.6. Sometimes amphibole from the Am + Qtz
235 symplectite shows a higher Al content (Al_2O_3 up to 15 wt%: ferropargasite to tschermakite).
236 Amphibole (Am_{2b}) from the Cpx + Pl ± Am symplectite is Mg-hornblende with low Na_2O (< 1.2
237 wt%) and X_{Mg} = 0.58-0.75.

238 Amphibole from the matrix shows a wide variability in composition depending on the specific
239 microstructural site (Fig. 6). Amphibole from the matrix is generally zoned with a Mg-hornblende
240 (or pargasite) core surrounded by a Al-poorer Mg-hornblende or actinolite thin rim. The Mg-
241 hornblende core locally shows a relatively high concentration of titanium as compared to the rim.
242 When matrix amphibole occurs near to the garnet crystals (Am_{3b}), the amphibole develops a thin
243 rim, similar to a halo, which is strongly enriched in Al_2O_3 (Al_2O_3 up to 14-15 wt%) (Mg-
244 hornblende, pargasite, to Fe-pargasite with X_{Mg} =0.44- 0.52, Na_2O up to 2.5 wt% and TiO_2 < 1.2
245 wt%). The matrix amphibole is locally overgrown by a later, thin rim of actinolite (Am_4). Finally,
246 semiquantitative analyses on amphibole filling garnet fractures revealed moderately high Al_2O_3
247 content (13-14 wt%), low TiO_2 (~0.3 wt%), and significant amount of Na_2O (~2 wt%). Amphibole
248 in the fractures of garnet has X_{Mg} ratio near to 0.3.
249 *Plagioclase* - Plagioclase in the Pl_1 + Ep_1 inclusions in garnet are difficult to analyze due to their
250 very small size. Pl_1 from a few samples have shown a very wide range of compositions from
251 andesine to bytwonite (X_{Na} from 0.13 to 0.68). Plagioclase (Pl_{2a}) associated to clinopyroxene and
252 amphibole in the symplectite is Na-rich ($X_{Na} \geq 0.80$), with compositions between oligoclase and
253 albite. Plagioclase (Pl_{2b}) associated to biotite, growing at the expense of former phengite, has a
254 composition between andesine and oligoclase, with X_{Na} = 0.63-0.79. Plagioclase (Pl_3) from the
255 coronitic microstructures is oligoclase with X_{Na} = 0.70-0.77. A plagioclase which is almost pure
256 albite (Pl_4), is also frequently found in the rock matrix.
257 *Biotite* - Biotite droplets and lamellae (Bt_1) growing with fine-grained plagioclase (Pl_{2b}) has an
258 intermediate composition between phlogopite and annite with TiO_2 ~2 wt% and X_{Mg} in the 0.52-
259 0.58 range. Biotite from the matrix (Bt_2) growing on garnet in sample FC9 shows a similar
260 composition, with comparable TiO_2 content and X_{Mg} ratio.
261 *Epidote* - Epidote belongs to the clinozoisite–epidote series. Two main compositional types (Fe-
262 poor and Fe-rich) have been observed enclosed in garnet crystals. Fe-poor epidote (Ep_{1a}), with
263 Fe_2O_3 content in the 1-3 wt% range and X_{Fe} ~ 0.05 [X_{Fe}= Fe/(Fe+Al)], is a clinozoisite. Fe-rich

epidote (Ep_{1b}) with a Fe_2O_3 content of 6.8-7.5 wt% and $X_{Fe} \sim 0.15$ is much more common. Epidote inclusions in garnet associated to Pl_1 belong to the Fe-rich epidote type.

Other minerals: ilmenite often contains significant amount of manganese. Chlorite replacing biotite reveals an intermediate composition between clinochlore and chamosite with TiO_2 below the detection limit, low MnO (0.2 wt%) and X_{Mg} ratio near to 0.67.

Results

Metamorphic evolution and reaction history

Based on mineral assemblages and microstructures the following metamorphic stages can be identified (Fig. 7).

Stage I: A HP, eclogite-facies, stage is revealed by the widespread occurrence of armoured relics of Na-rich clinopyroxene (omphacite, Cpx_1) enclosed in garnet. Garnet porphyroblasts also contains several inclusions of amphibole (Am_1), epidote (Ep_1), rutile and ilmenite, which can be considered in equilibrium with garnet being often idioblastic. The occurrence of plagioclase (Pl_1), systematically associated to epidote in polymineralic inclusions within garnet, may be interpreted as related to dehydration reactions which occurred in a confined chemical domain, as already suggested by Cortesogno et al. (2004) for similar microstructures. A plausible reaction might be such as: clinozoisite/zoisite + quartz = anorthite + garnet + fluid (Holdaway 1966; Nitsch and Winkler 1965).

Although phengite was not observed in the studied rocks, the occurrence of phengite in the HP assemblage is inferred from the biotite + plagioclase symplectites, likely derived from the breakdown of former phengite (e.g. Groppo et al. 2007a,b; Vrabec et al. 2012). The slightly preserved garnet zoning (i.e. progressive increase in pyrope and decrease in grossularite components from the core to the rim) suggests that garnet growth occurred during increasing

pressure and temperature, as previously documented for other Variscan granulitized eclogites (e.g. Cruciani et al. 2012; O'Brien 1997).

Stage II: This stage is characterized by the breakdown of omphacite with the formation of two different symplectite types: (i) amphibole (Am_{2a}: pargasite/Mg-hornblende) + quartz symplectite, and (ii) clinopyroxene (Cpx_2) + plagioclase (Pl_{2a}: oligoclase/albite) ± amphibole (Am_{2b}: Mg-hornblende) symplectite.

The Am_{2a} + Qtz symplectite always replaces omphacite included in garnet. This symplectite type, already described in the literature, probably derives from Hbl + Qtz exsolved from non-stoichiometric pyroxene (e.g. Anderson and Moecher 2007). The precursor pyroxene is interpreted as supersilicic; it apparently exsolved SiO_2 (and amphibole) and left a stoichiometric pyroxene behind.

The $Cpx_2 + Pl_{2a} \pm Am_{2b}$ symplectite, by far the most abundant in the studied rocks, is widespread in the rock matrix where omphacite is completely consumed, and very common also inside the garnet, where omphacite relics are still preserved. The following balanced reaction describes the omphacite breakdown into the Cpx + Pl ± Am symplectite (matrix of residuals is given in the Supplementary material):

(1) $0.85\ Cpx_1 + 0.002\ H_2O = 0.31\ Pl_{2a} + 0.41\ Cpx_2 + 0.002 Am_{2b}$

Due to the late pervasive growth of amphibole at the expenses of the symplectite, the modal proportion of symplectitic minerals is difficult to estimate. The modal amount of amphibole in the symplectite is strongly variable depending on the specific microdomain, but it is < 10 vol%. We also attribute to the symplectite stage the formation of the biotite (Bt_1) + plagioclase (Pl_{2b}) symplectites (Fig. 3b) which have been observed only in the rock matrix, and that likely derived from the breakdown of former phengite. The chronological relationships among the Am_{2a} + Qtz, the $Cpx_2 + Pl_{2b} \pm Am_{2b}$ and the $Bt_1 + Pl_{2b}$ symplectites are difficult to ascertain, mainly because each symplectite type develops in a specific reacting microdomain. However, we suggest that the

three symplectite types should be almost coeval, being likely derived from synchronous breakdown of omphacite and phengite, respectively.

Stage III: This stage is characterized by the widespread formation of amphibole that represents by far the most abundant mineral in the studied rocks. The growth of amphibole implies that H_2O was available in the system at this metamorphic stage. This hydration stage led to the development of zoned amphibole porphyroblasts in the rock matrix and to the formation of a thin green amphibole layer around garnet (Am_{3b}, Mg-hornblende/pargasite/tschermakite, strongly enriched in Al_2O_3 as compared to other amphibole types). The amphibole layer at the interface between garnet and the surrounding matrix locally assumes the aspect of a discontinuous corona consisting of amphibole and subordinate coronitic plagioclase (Pl_3).

The matrix amphibole most likely developed, together with coronitic plagioclase, through a reaction involving symplectitic minerals and garnet as reactants (matrix of residuals is given in the Supplementary material):

(2a) $0.69\ Pl_{2a} + 0.14\ Cpx_2 + 0.07\ Grt_{rim} + 0.07\ H_2O = 0.66\ Pl_3 + 0.07\ Am_{3(matrix)} + 0.19\ Qtz$

On its turn, the Al-rich amphibole layer in contact with garnet probably formed from a reaction that involved garnet and some of the coronitic plagioclase formed by reaction (2a):

(2b) $0.32\ Grt_{rim} + 0.30\ Pl_3 + 0.84\ H_2O = 0.29\ Am_{3b}$.

Stage IV: This stage is documented by the development of actinolite rim around amphibole porphyroblasts, and by the growth of albite, chlorite, and epidote in garnet and in the matrix. We attribute to this stage also the growth of late biotite flakes at the expense of garnet or along the cleavages of matrix amphibole, the growth of chlorite at the expense of biotite, and the titanite partially replacing ilmenite.

P-T pseudosection modeling

339 The metamorphic evolution of the amphibolitized eclogites has been reconstructed using the
340 petrologic approach of isochemical phase diagrams. Five samples were investigated for P-T
341 pseudosection modelling but the results for sample FC9 are discussed in detail. P–T pseudosections
342 were calculated using PerpleX_6.6.7 (Connolly 1990, 2009) and the internally consistent
343 thermodynamic data set and the equation of state for H_2O by Holland and Powell (1998, revised
344 2004). The phases considered in the calculation are amphibole, biotite, K-white mica,
345 clinopyroxene, orthopyroxene, garnet, plagioclase, epidote, ilmenite, rutile, quartz, lawsonite,
346 chlorite and titanite. Solid solution models are those of Holland and Powell (1998) for garnet, white
347 mica and epidote, Holland and Powell (1996) for orthopyroxene, Green et al. (2007) for
348 clinopyroxene, Holland et al. (1998) for chlorite, Dale et al. (2005) for amphibole and Newton et al.
349 (1981) for plagioclase. Since garnet contains very low and homogeneous spessartine component
350 (MnO < 3 mol.%), MnO was neglected in the model system. All the pseudosections have been
351 calculated at $aH_2O = 1.0$. However, the effects on the pseudosection topology of a lower aH_2O have
352 been also investigated.
353 Each metamorphic stage was modeled by using a P-T pseudosection calculated for a specific bulk
354 composition. The HP stage (stage I) was modeled using the whole-rock bulk composition of a
355 selected sample, obtained by XRF (Table 2): chemical fractionation effects due to the growth of
356 garnet porphyroblasts have been considered negligible because garnet is almost unzoned. Stages II
357 and III were modeled using the composition of the effective reacting microdomains (Table 2)
358 according to the method described in Cruciani et al. (2008c). The method is based on the calculation
359 of the balanced reactions involved in the formation of the symplectitic / coronitic microstructures
360 using the measured compositions of both reactants and products (see the previous "Metamorphic
361 evolution and reaction history "section). The modeled balanced reactions are successful if they are
362 consistent with the observed microstructures (i.e. inferred reactants and products should appear on
363 opposite sides of the model reactions), and if the stoichiometric coefficients of the reactions are in
364 agreement with the observed amounts of mineral products. The accuracy of the result is given by

365 the absolute value of residuals, which should be as low as possible. The input bulk composition to
366 be used for the pseudosection calculation is obtained by combining the stoichiometric coefficients
367 of the products with their measured chemical compositions.
368 *Stage I (HP stage):* The HP stage has been modeled in the NCKFMASTHO model system by a P–T
369 pseudosection calculated in the P-T range 500-950°C, 0.1-2.5 GPa. CaO was reduced according to
370 P_2O_5 content in the rock, on the likelihood assumption that phosphorus binds exclusively to calcium
371 in ideally-composed apatite. Owing to the abundance of epidote inclusions in garnet core, a Fe_2O_3 =
372 10% of FeO_{tot} has been considered in the calculation. This value has been set arbitrarily, basing on
373 the modal abundance of Fe^{+3}-bearing minerals: however, calculations with all iron as Fe^{2+} do not
374 substantially change the P-T pseudosection topology, a part from the stabilization of
375 zoisite/clinozoisite instead of epidote.
376 The calculated P–T pseudosection (Fig. 8a) is dominated by tri-, quadri- and penta-variant fields,
377 with a large hexa-variant field confined at HP conditions. K-white mica (Wmca) is stable at
378 pressures above 1.1 GPa, whereas garnet appears at pressure as low as 0.9 GPa for intermediate
379 temperature values. Orthopyroxene is stable at low-P and high-T conditions. Multivariant fields at
380 high-P/low-T conditions are characterized by the coexistence of clinopyroxene and lawsonite.
381 Epidote is stable in most of the multivariant fields within the pressure range 0.6 GPa <P< 1.8 GPa
382 at T <650°C.
383 The observed HP assemblage (Cpx_1+Grt+Qtz+Am_1+Wmca+Ep_1+Rt±Ilm) matches the modeled
384 quadri-variant fields Cpx+Wmca+Grt+Ep+Qtz+Ilm and Cpx+Wmca+Grt+Ep+Qtz+Rt, and the tri-
385 variant field which separates the aforementioned quadri-variant fields (i.e.
386 Cpx+Wmca+Grt+Ep+Qtz+Rt+Ilm), stable at 1.3 < P < 1.8 GPa and 580 < T < 640°C (red area in
387 Fig. 8). Plagioclase, locally found as polymineralic Ep_1+Pl_1 inclusions in garnet poikiloblasts, is not
388 compatible with these P-T conditions, suggesting that it probably represents the product of
389 dehydration reactions in a confined domain (see before). These P-T conditions are further
390 constrained by the garnet and clinopyroxene compositional isopleths (Figs. 8b,c,d). The modeled

391 compositional isopleths (X_{Mg} and X_{Ca} in Grt: Fig. 8b,c; X_{Na} in Cpx: Fig. 8d) show, in fact, a good
392 correspondence with the mineral compositions actually measured in sample FC9 (Grt: X_{Ca}=0.26-
393 0.30; X_{Mg}=0.10-0.16; Cpx_1: X_{Na}=0.43-0.47; Table 1) (red area in Fig. 8). Although the very slight
394 compositional zoning of garnet does not allow to distinguish between P-T conditions of the garnet
395 core and those of the garnet rim, the progressive increase in pyrope and decrease in grossularite
396 components from core to rim, suggest that garnet grew in response to a temperature increase.
397 Application of the Grt-Cpx geothermometer (Krogh Ravna 2000 and Powell 1985 calibrations)
398 applied to the composition of garnet core and omphacite from sample FC9 (after normalization for
399 Fe^{3+} content in garnet and omphacite) yielded temperature of ~670°C at P around 1.5GPa (Fig. 8).
400 For the same pressure, the calibration by Pattison and Newton (1989) gave temperature ~600°C
401 which fit very well with the results of the P-T pseudosection modeling (Fig. 8).
402 *Stage II (Symplectite stage):* The Cpx_2 + Pl_{2a} + Am_{2b} symplectites resulted from metamorphic
403 reactions occurring at the scale of small domains, not represented by the whole-rock bulk
404 composition. To model the P–T conditions at which these symplectites formed, the method of
405 Groppo et al. (2007a,b) was applied (see also Cruciani et al. 2008c, 2011). In the calculation, all
406 iron was assumed to be divalent; K and Ti were neglected because K- and Ti-bearing phases do not
407 occur in the symplectites. The correspondent P–T pseudosection calculated in the P-T range 550-
408 850°C, 0.6-1.9 GPa is shown in Fig. 9. The pseudosection is dominated by quadri- and tri-variant
409 fields, with some minor divariant fields at intermediate P-T conditions and pentavariant fields at
410 low P conditions. Clinopyroxene is stable in all the multivariant fields of the P-T pseudosection.
411 Very small amounts of garnet (< 5 vol%) and quartz (< 5 vol%) are stable in the P-T region of
412 interest. The plagioclase-in curve has a positive slope, being the temperature of appearance for this
413 mineral strongly dependent on pressure values. The maximum temperature of amphibole stability
414 field is strongly dependent on pressure; anyway, amphibole is not stable, for the composition of
415 interest, at T > 800°C (Fig. 9).

The symplectite assemblage (Cpx_2+Pl_2+Am_{2b}) matches the quadri- and penta-variant fields characterized by the occurrence of amphibole + clinopyroxene + plagioclase ± minor amounts of quartz (< 3 vol%) (this last is probably an artifact due to a slightly high SiO_2 content in the input bulk-composition, but does not limit the validity of the results). The P–T conditions at which the symplectite assemblage grew are constrained at ~1.25-1.40 GPa and 650-710°C (area in Fig. 9) by the Pl_2 and Cpx_2 compositions (Pl_{2a}: X_{Na} = 0.80–0.82, Cpx_2: X_{Mg} = 0.67-0.69), coupled with the measured Si content of amphibole (Si ~6.9-7.0 a.p.f.u) (Fig. 9). The modeled isomodes predict that, at these P-T conditions, amphibole (Fig. 9) could be as low as 1 vol.% with a maximum possible content of 10 vol.% .

Stage III: The corona-type microstructures consisting of amphibole and plagioclase have been modeled following the method of Groppo et al. (2007a) and Cruciani et al. (2012) (see also Adjerid et al., 2013). In the calculation, all iron was assumed to be divalent; K and Ti were neglected because K- and Ti-bearing phases do not occur in the corona-type microstructures. The correspondent P–T pseudosection calculated in the P-T range 550-850°C, 0.6-1.9 GPa is shown in Fig. 10. The pseudosection is dominated by di-, tri-, and quadri-variant fields. Clinopyroxene is stable in most of the multivariant fields except those at low-P and low-T conditions. Orthopyroxene is stable at high-T, low-P, whereas garnet is stable in most of the P-T fields, except those at low P. The amphibole–out curve has an irregular shape, with amphibole stable in almost all the multivariant fields occurring at P < 1.5 GPa.

The stage III mineral assemblage (Am_3 + Pl_3 ± Qtz) matches different modeled multivariant fields characterized by the occurrence of amphibole + plagioclase ± minor amounts of the reactants (garnet and clinopyroxene). The P–T conditions at which this assemblage formed are constrained at 600-670°C, P=0.65-0.95 GPa (area in Fig. 10) based on the comparison of the measured Pl_3 and Am_3 compositions in sample FC9 (Pl_3: X_{Na} = 0.70–0.71, Am_3: Si~6.8-6.9 a.p.f.u.) with the modeled compositional isopleths (Fig.10). The modeled isomodes predict that quartz and garnet occur in very small modal amounts (≤ 6 vol.% and < 3 vol.%, respectively) at the constrained P-T conditions

(Fig. A4 supplementary material). These P-T conditions have been further confirmed by applying the Hbl-Pl geothermometer of Holland and Blundy (1994) to the same assemblage (Fig. 10). Lowering the aH_2O to 0.5 resulted in a shift of ~ 60°C and ~ 1 kbar for all the field boundaries and compositional isopleths toward lower temperature and pressure.

Discussion

The P-T path of the Giuncana eclogite

The P–T path of the retrogressed eclogite from Giuncana, and the P-T paths of the other Sardinian eclogites, are reported in Fig. 11. The first portion of the calculated P–T path reflects an increase in temperature accompanied by a decrease in pressure from the HP stage under eclogite-facies conditions (570-670 °C, 1.4-1.9 GPa at aH_2O=1.0) to the symplectite stage under upper amphibolite/granulite-facies conditions (660-730°C; ~ 1.30-1.45 GPa at aH_2O=1.0). The same stages, recalculated at aH_2O=0.5, are shifted of ~30-60 °C toward lower T with respect to the estimates obtained with aH_2O=1 (Fig. 11). After the peak of metamorphism, corresponding to the symplectite formation, the sample experienced a significant re-equilibration at the transition between granulite- and upper amphibolite-facies conditions (~660-750°C, ~1.0-1.35 GPa at aH_2O=1.0) with formation of the corona-type microstructures. This stage, recalculated at aH_2O=0.5, is located at ~ 60 °C and ~1 kbar lower that the estimates obtained with aH_2O=1 (Fig. 11).

Comparing the P-T trajectory obtained for the Giuncana eclogites with the P–T paths of the eclogites from different localities in NE Sardinia (Punta Orvili: Cruciani et al. 2011; Punta de Li Tulchi: Cruciani et al. 2012; Golfo Aranci: Giacomini et al. 2005a; Fig. 11), it appears that the eclogites from Giuncana do not preserve the prograde segment of the P-T path. Except for the prograde part, the P-T path of the eclogites from Giuncana is similar to the P-T path deduced for the Punta Orvili metabasite (Cruciani et al. 2011), which also belongs to the L-MGMC and crops out

very close to the Posada-Asinara shear zone. Furthermore, peak temperatures obtained for the Giuncana eclogites are lower than those obtained for the eclogites embedded in the HGMC (Punta de li Tulchi eclogite, Cruciani et al. 2012: peak temperature in excess of 800°C; retrogressed eclogite of Golfo Aranci, Giacomini et al. 2005a: peak metamorphism ~700-800°C).

The Giuncana eclogite within the Variscan geology

The metabasites with relics of eclogite-facies assemblages in north Sardinia have a good deal of features in common with other sectors of the southern Variscan Realm. The protolith age of Sardinian eclogites seems to be Middle Ordovician, as suggested by four U-Pb zircon ages of Punta de Li Tulchi (453 ± 14 Ma), Golfo Aranci (460 ± 5 Ma), and Giuncana (454 ± 6 Ma) eclogites, obtained by Palmeri et al. (2004), Giacomini et al. (2005a) and Cruciani et al. (2013b), respectively. As concerning the age of HP metamorphism, it is not well constrained neither in the Giuncana eclogite nor in the other eclogite localities in Sardinia. Palmeri et al. (2004), on the basis of SHRIMP zircon U-Pb data on the Punta de Li Tulchi eclogite (HGMC), put forward the hypothesis that 400 ± 10 Ma might be the age of the eclogite formation in NE Sardinia. However, according to these Authors, this age could also represent the result of Pb loss during the Variscan event.In the Golfo Aranci eclogites (HGMC), Giacomini et al. (2005a) obtained a U-Pb zircon age of 352±3Ma. According to these Authors, it is difficult to assess whether this age is related to the eclogitic or to the post-eclogitic metamorphic equilibration. Later, Giacomini et al. (2005b) interpreted Early Visean zircon ages of retrogressed eclogites embedded in HGMC as related to HP, eclogite-facies, metamorphic overprint.

The geochemical signature of the different mafic bodies points to MORB and N-MORB protoliths (Cappelli et al. 1992; Cortesogno et al. 2004) and in one case alkaline within-plate alkali basalts (Cruciani et al. 2010).

493 Cruciani et al. (2010) interpreted the metabasite with eclogite relics with a MORB-type affinity as
494 the product of rifting and opening of a small extensional basin within the northern Gondwana
495 margin. These metabasites are enclosed within two tectono-metamorphic complexes, which reflect
496 different tectono-thermal evolutions:
497 (i) The HGMC consists of anatexites hosting several hectometric bodies of metabasites, including
498 layered mafic complexes with ultramafic cumulates, metabasalts and leptyno-amphibolite. The HP
499 metabasites (e.g. Punta de li Tulchi), before the retrogression into low-P amphibolite-facies
500 conditions, experienced an eclogite-facies stage at 1.6-2.1 GPa, 660-700 °C, followed by a
501 granulite-facies equilibration with temperature in excess of 800 °C, and pressure in the range 1.0-
502 1.3 GPa (Cruciani et al. 2012). The highest P-T conditions determined in the migmatite from the
503 HGMC are those obtained in amphibole-bearing migmatites by Massonne et al. (2013), i.e. 700°C
504 and 1.3 GPa, interpreted as the P-T conditions of partial melting.
505 (ii) A different, cooler evolution predating the Barrovian stage, characterizes the L-MGMC, where
506 LT/HP metamorphic conditions, have been documented based on the occurrence of phengite in
507 metapelite (Cruciani et al. 2013); moreover, close to the Giuncana eclogite, kyanite-bearing
508 selvages, possibly eclogitic remnant, are preserved in quartz veins within the staurolite-bearing
509 micaschists. Even though the thermal peak of the Giuncana eclogite occurred at temperatures lower
510 than that recorded by the eclogites embedded in HGMC (Fig. 11) an increase in temperature is
511 required for the formation of the symplectite in the Giuncana eclogite, which was previously
512 exhumed at middle crustal level. The heat transfer responsible for the temperature increase could be
513 associated to the extrusion of heated orogenic lower crust over the middle crust of the L-MGMC.
514 The P-T conditions experienced by the mafic bodies of the axial zone of the Sardinia Variscides,
515 their chemical signature and their structural location within two complexes with different tectono-
516 thermal evolution, have much in common with other sectors of the southern Variscides, such as the
517 Central Iberia Zone, the French Massif Central, the Bohemian Massif and western Tatra. In these
518 Variscan sectors, partially molten orogenic lower crust is extruded over mid-crustal levels

519 generating a reversal metamorphic gradient (Moussallam et al. 2012; Pitra et al. 2010; Štípská et al.
520 2008). Whether the occurrence of MORB-derived eclogites within granulitic continental complexes
521 could mark or not an oceanic suture in the south Variscan branch is a matter of debate (Arenas et
522 al. 2007; Burg et al. 2004; Lexa et al. 2011; Štípská et al. 2004, 2006). Several authors claimed the
523 subduction of oceanized basins (Palaeothethys, South Armorican Ocean, Medio-Europen Ocean)
524 beneath the group of small continental plates interposed between Gondwana and Laurussia, from
525 Silurian to early Carboniferous (Matte 2001; Pin 1990; Tait et al. 1997; von Raumer et al. 2009,
526 2012; von Raumer and Stampfli 2008) prior to their collision and amalgamation into the incoming
527 Pangaea. These basins are interpreted as back-arc basins (Fig. 12a) resulted from the retreat of the
528 Rheic slab below Gondwana (Gaggero et al. 2012; Ribeiro et al. 2007; Rossi et al. 2009). However
529 the existence of these basins, their width and their eventual north directed subduction ending in the
530 collision with Armorica and/or other intervening terranes between Gondwana and Laurussia are still
531 debated; as a consequence, the interpretation of the MORB-type eclogites in the HP units
532 transported toward the north Gondawana margin as remnants of such basins is still not definitively
533 proved. Actually the provenance of the HP metabasites in the southern Variscan branch is a
534 puzzling issue. For instance, Schulmann et al. (2005, 2009) and Lexa et al. (2011) consider the HP
535 metabasite in the Moldanubian Zone as derived from the Rheic oceanic lithosphere of the
536 Saxothuringian Zone by underplating beneath the Teplá–Barrandian terrane. In such a picture the
537 Giuncana eclogite and its host micaschists can only tentatively placed within a geodynamic frame,
538 which implies the subduction of a small back-arc basin, formed in the upper Ordovician-early
539 Silurian, beneath "Armorica", coherently with the southern vergence of the Sardinia Variscan
540 orogenic wedge (Fig. 12b). The Giuncana eclogite, hence, could be referred to an accretionary
541 prism (Fig.12b) exhumed at mid-crustal levels during the D_1 deformation event and later overridden
542 by horizontally extruded, partially melted, hot orogenic lower-crust that caused its equilibration
543 under an inverted thermal gradient during the D_2 deformation phase. Whether the thermal flow
544 responsible for the amphibolitic-granulitic event post-dating the eclogitic stage recorded in the

545 Giuncana eclogite is to be referred to the slab break-off (Fig.12.c) (Casini et al. 2013; Janoušek and
546 Holub 2007) also responsible for the production of Mg-K suite as in the Bohemian Massif and in
547 Corsica, or to radiogenic heating (Pitra et al. 2010) has to be further constrained.
548
549 **Acknowledgements**
550 Financial support was provided by Regione Autonoma della Sardegna, Progetti di Ricerca di base
551 orientata, L.R. 7/2007- annualità 2010 (M. Franceschelli). The authors wish to thanks Janák M.
552 (Slovak Academy of Sciences) and Schulz B. (Wurzburg University) for their helpful comments
553 and constructive criticism.
554
555
556
557 **References**
558 Adjerid Z, Godard G, Ouzegane K, Kienast J-R (2013) Multistage progressive evolution of rare
559 osumilite-bearing assemblages preserved in ultrahigh-temperature granulites from In Ouzzal
560 (Hoggar, Algeria). J metam Geol 31:505–524
561 Anderson ED, Moecher DP (2007) Omphacite breakdown reactions and relation to eclogite
562 exhumation rates. Contrib Mineral Petrol 154:253–277
563 Arenas R, Martínez Catalán JR, Sánchez Martínez S, Fernández-Suárez J, Andonaegui P, Pearce
564 JA, Corfu F (2007) The Vila de Cruces Ophiolite: a remnant of the Early Rheic Ocean in the
565 Variscan suture of Galicia (Northwest Iberian Massif). J Geol 115:129–148
566 Burg JP, Kaus BJP, Podladchikov YY (2004) Dome structures in collision orogens: Mechanical
567 investigation of the gravity/compression interplay, in Whitney, D.L., et al., eds., Gneiss domes in
568 orogeny: Geol Soc Am Special Paper 380:47–66
569 Cappelli B, Carmignani L, Castorina F, Di Pisa A, Oggiano G, Petrini R (1992) A Hercynian suture
570 zone in Sardinia: geological and geochemical evidence. Geodin Acta 5:101–118

571 Carmignani L, Carosi R, Di Pisa A, Gattiglio M, Musumeci G, Oggiano G, Pertusati PC (1994) The
572 Hercynian chain in Sardinia (Italy). Geodin Acta 7(1):31–47
573 Carosi R, Oggiano G (2002) Transpressional deformation in northwestern Sardinia (Italy): insights
574 on the tectonic evolution of the Variscan belt. C R Geoscience 334:287–294
575 Carosi R, Montomoli C, Tiepolo M, Frassi C (2012) Geochronological constraints on post-
576 collisional shear zones in the Variscides of Sardinia (Italy). Terra Nova 24:42–51
577 Casini L, Funedda A, Oggiano G (2010) A balanced foreland-hinterland deformation model for the
578 Southern Variscan belt of Sardinia, Italy. Geol J 45:634–649
579 Casini L, Puccini A, Cuccuru S, Maino M, Oggiano G (2013) GEOTHERM: A finite difference
580 code for testing metamorphic P–T–t paths and tectonic models. Computers & Geosciences 59:
581 171–180
582 Connolly JAD (1990) Multivariable phase diagrams: an algorithm based on generalized
583 thermodynamics. Am J Sci 290:666–718
584 Connolly JAD (2009) The geodynamic equation of state: what and how. Geochemistry,
585 Geophysics, Geosystems 10, Q10014
586 Cortesogno L, Gaggero L, Oggiano G, Paquette JL (2004) Different tectono-thermal evolutionary
587 paths in eclogitic rocks from the axial zone of the Variscan chain in Sardinia (Italy) compared
588 with the Ligurian Alps. Ofioliti 29:125–144
589 Cruciani G, Dini A, Franceschelli M, Puxeddu M, Utzeri D (2010) Metabasite from the Variscan
590 belt in NE Sardinia, Italy: within-plate OIB-like melts with very high Sr and low Nd isotope
591 ratios. Eu J Mineral 22:509–523
592 Cruciani G, Franceschelli M, Elter FM, Puxeddu M, Utzeri D (2008a) Petrogenesis of Al-silicate-
593 bearing throndhjemitic migmatites from NE Sardinia, Italy. Lithos 102:554–574
594 Cruciani G, Franceschelli M, Groppo C (2011) P-T evolution of eclogite-facies metabasite from NE
595 Sardinia, Italy: insights into the prograde evolution of Variscan eclogites. Lithos 121:135–150

596 Cruciani G, Franceschelli M, Groppo C, Brogioni N, Vaselli O (2008c) Formation of clinopyroxene
597 + spinel and amphibole+spinel symplectites in coronitic gabbros from the Sierra de San Luis
598 (Argentina): a key to post-magmatic evolution. J metam Geol 26:759–774
599 Cruciani G, Franceschelli M, Groppo C, Spano ME (2012) Metamorphic evolution of non-
600 equilibrated granulitized eclogite from Punta de li Tulchi (Variscan Sardinia) determined through
601 texturally controlled thermodynamic modeling. J metam Geol 30:667–685
602 Cruciani G, Franceschelli M, Jung S, Puxeddu M, Utzeri D (2008b) Amphibole-bearing migmatites
603 from the Variscan Belt of NE Sardinia, Italy: Partial melting of mid-Ordovician igneous sources.
604 Lithos 105:208–224
605 Cruciani G, Franceschelli M, Massonne H-J, Carosi R, Montomoli C (2013) Pressure–temperature
606 and deformational evolution of high-pressure metapelites from Variscan NE Sardinia, Italy.
607 Lithos 175–176:272–284
608 Cruciani G, Franceschelli M, Langone A, Spano ME (2013b) Nature and age of protolith of
609 retrogressed eclogite from the Variscan basement of north-central Sardinia, Italy. X International
610 Eclogite Conference, Abstract volume, p. 20.
611 Dale J, Powell R, White RW, Elmer FL, Holland JB (2005) A thermodynamic model for Ca-Na
612 clinoamphiboles in Na_2O–CaO–FeO–MgO–Al_2O_3–SiO_2–H_2O–O for petrological calculations. J
613 metam Geol 23:771–791
614 Del Moro A, Di Pisa A, Oggiano G, Villa IM (1991) Isotopic ages of two constrained
615 tectonometamorphic episode in the Variscan chain in N Sardinia. Geologia del basamento
616 Italiano. 21- 22 marzo 1991, Siena, 33–35
617 Denele Y, Olivier Ph, Gleizes G, Barbey P (2007) The Hospitalet gneiss dome (Pyrenees) revisited:
618 lateral flow during Variscan transpression in the middle crust. Terra Nova 19:445–453
619 Elter FM, Musumeci G, Pertusati PC (1990) Late Hercynian shear zone in Sardinia. Tectonophysics
620 176:387–404

621 Eltrudis A, Franceschelli M, Gattiglio M, Porcu R (1995) Discontinuous metamorphic zonation in
622 the Paleozoic units of the Hercynian chain of SW Sardinia, Italy: Evidence from structural and
623 illite crystallinity data. Schweiz Mineral Petrog Mitt 75:201–211
624 Faryad SW, Jedlicka R, Collett S (2013) Eclogite facies rocks of the Monotonous unit, clue to
625 Variscan suture in the Moldanubian Zone (Bohemian Massif). Lithos 179:353-363
626 Franceschelli M, Carcangiu G, Caredda AM, Cruciani G, Memmi I, Zucca M (2002)
627 Transformation of cumulate mafic rocks to granulite and re-equilibration in amphibolite and
628 greenschist facies in NE Sardinia, Italy. Lithos 63:1–18
629 Franceschelli M, Pannuti F, Puxeddu M (1990) Texture development and PT time path of
630 psammitic schists from the Hercynian chain of NW Sardinia (Italy). Eu J Mineral 2:385–398
631 Franceschelli M, Puxeddu M, Cruciani G (2005) Variscan metamorphism in Sardinia, Italy: review
632 and discussion. In: Carosi, R., Dias, R., Iacopini, D., Rosenbaum, G. (Eds.), The Southern
633 Variscan Belt. J Virtual Explorer 19, Paper 2
634 Franceschelli M, Puxeddu M, Cruciani G, Utzeri D (2007) Metabasites with eclogite facies relics
635 from Variscides in Sardinia, Italy: a review. Int J Earth Sci 96:795–815
636 Frassi C, Carosi R, Montomoli C, Law RD (2009) Kinematics and vorticity of flow associated with
637 postcollisional oblique transpression in the Variscan Axial Zone of northern Sardinia (Italy). J
638 Structural Geol 31:1458–1471
639 Gaggero L, Oggiano G, Funedda A, Buzzi L (2012) Rifting and Arc-Related Early Paleozoic
640 Volcanism along the North Gondwana Margin: Geochemical and Geological Evidence from
641 Sardinia (Italy). J Geol 120:273–292
642 Gébelin A, Roger F, Brunel M (2009) Syntectonic crustal melting and high-grade metamorphism in
643 a transpressional regime, Variscan Massif Central, France. Tectonophysics 477:229–243
644 Giacomini F, Bomparola RM, Ghezzo C (2005a) Petrology and geochronology of metabasites with
645 eclogite facies relics from NE Sardinia: constraints for the Palaeozoic evolution of Southern
646 Europe. Lithos 82:221–248

647 Giacomini F, Dallai L, Carminati E, Tiepolo M, Ghezzo C (2008) Exhumation of a Variscan
648 orogenic complex: insights into the composite granulitic–amphibolitic metamorphic basement of
649 Southeast Corsica (France), J metam Geol 26:403–436
650 Giacomini F, Tiepolo M, Tribuzio R (2005b) 10 micron excimer laser ablation U/Pb geochronology
651 on zircons from kyanite- and zoisite-bearing eclogites of Sardinia and Liguria: new constraints to
652 the variscan Orogeny. FIST, Federazione Italiana di Scienze della Terra, Epitome Geoitalia
653 2005, Quinto Forum Italiano di Scienze della Terra. Spoleto, 21–23 settembre 2005
654 Green ECR, Holland TJB, Powell R (2007) An order-disorder model for omphacitic pyroxenes in
655 the system jadeite-diopside-hedembergite-acmite, with applications to eclogitic rocks. Am
656 Mineral 92:1181–1189
657 Groppo C, Lombardo B, Rolfo F, Pertusati PC (2007a) Clockwise exhumation path of granulitized
658 eclogites from the Ama Drime range (Eastern Himalayas). J metam Geol 25:51–75
659 Groppo C, Lombardo B, Castelli D, Compagnoni R (2007b) Exhumation history of the UHPM
660 Brossasco-Isasca Unit, Dora-Maira Massif, as inferred from a phengite amphibole eclogite. Int
661 Geol Rev 49:142–168
662 Holdaway MJ (1966) Hydrothermal stability of clinozoisite plus quartz. Am J Sci 264:643–667
663 Holland TJB, Blundy J (1994) Non-ideal interactions in calcic amphiboles and their bearing on
664 amphibole-plagioclase thermometry. Contrib Mineral Petrol 116:433–447
665 Holland TJB, Powell R (1996) Thermodynamics of order-disorder in minerals, 2. Symmetric
666 formalism applied to solid solutions. Am Mineral 81:1425–1437
667 Holland TJB, Powell R (1998) An internal consistent thermodynamic dataset for phases of
668 petrologic interest. J metam Geol 16:309–343
669 Holland TJB, Baker JM, Powell R (1998) Mixing properties and activity-composition relationships
670 of chlorites in the system MgO-FeO-Al_2O_3-SiO_2-H_2O. Eu J Mineral 10:395–406

671 Janoušek V, Holub FV (2007) The causal link between HP-HT metamorphism and ultrapotassic
672 magmatism in collisional orogens: case study from the Moldanubian Zone of the Bohemian
673 Massif. Proceedings of the Geologists association 118:75-86
674 Keppie JD, Nance RD, Murphy JB, Dostal J, Braid JA (2010) The high-pressure Iberian–Czech belt
675 in the Variscan orogen: Extrusion into the upper (Gondwanan) plate? Gondwana Res 17:306-316
676 Krogh Ravna E (2000) The garnet-clinopyroxene Fe^{2+}-Mg geothermometer: an updated calibration.
677 J metam Geol 18:211-219
678 Lardeaux JM, Ledru P, Daniel I, Duchene S (2001) The Variscan French Massif Central – a new
679 addition to the ultra-high pressure metamorphic "club": exhumation processes and geodynamic
680 consequences. Tectonophysics 332:143-167
681 Leake BE, Woolley AR, Arps CES (1997) Nomenclature of amphiboles: report of the
682 subcommittee on amphiboles of the International Mineralogical Association, commission on new
683 minerals and mineral names. Can Mineral 35:219–246
684 Lexa O, Schulmann K, Janousek V,Stıpska P, Guy A, Racek M (2011) Heat sources and trigger
685 mechanisms of exhumation of HP granulites in Variscan orogenic root. J metam Geol 29:79–102
686 Liou JG, Zhang RY, Ernst WG, Rumble D, Maruyama S (1998) High-pressure minerals from
687 deeply subducted metamorphic rocks. In: Hemley, R.J. (ed.), Ultrahigh-Pressure Mineralogy.
688 Rev in Mineralogy 37:33–96
689 Martínez Catalán JR (2011) Are the oroclines of the Variscan belt related to late Variscan strike-slip
690 tectonics? Terra Nova 23:241–247
691 Massonne H-J, Cruciani G, Franceschelli M (2013) Geothermobarometry on anatectic melts – a
692 high-pressure Variscan migmatite from northeast Sardinia. Int Geol Rev 55:1490-1505
693 Matte P (2001) The Variscan collage and orogeny (480–290 Ma) and the tectonic definition of the
694 Armorica microplate: a review. Terra Nova 13:122–128

695 Mogessie A, Ettinger K, Leake BE (2004) AMPH-IMA04 a revised Hypercard program to
696 determine the name of an amphibole from chemical analyses according to the 2004 International
697 Mineralogical Association scheme. Min Mag 68:825–830
698 Morimoto N (1988) Nomenclature of Pyroxenes. Mineral Petrol 39:55–76
699 Moussallam Y, Schneider DA, Janák M, Thöni M, Holm DK (2012) Heterogeneous extrusion and
700 exhumation of deep-crustal Variscan assembly: Geochronology of the Western Tatra Mountains,
701 northern Slovakia. Lithos 144–145:88–108
702 Newton RC, Charlu TV, Kleppa OJ (1981) Thermochemistry of the high structural state
703 plagioclases. Geochim Cosmochim Acta 44:933–941
704 Nitsch KH, Winkler HGF (1965) Bildungsbedingung von Epidot und Orthozoisit. Beitr Min Petr,
705 11:470-486
706 O'Brien PJ (1997) Garnet zoning and reaction textures in overprinted eclogites, Bohemian Massif,
707 European Variscides: a record of their thermal history during exhumation. Lithos 41:119–133
708 O'Brien PJ (2000) The fundamental Variscan problem: high-temperature metamorphism at different
709 depths and high-pressure metamorphism at different temperatures. In: Franke W, Haak V,
710 Oncken O, Tanner D (eds) Orogenic processes: quantification and modelling in the Variscan
711 belt. Geol Soc London Special Publ 179:369–386
712 Palmeri R, Fanning M, Franceschelli M, Memmi I, Ricci CA (2004) SHRIMP dating of zircons in
713 eclogite from the Variscan basement in north-eastern Sardinia (Italy). Neues Jahrb Mineral
714 Monat 6:275–288
715 Pattison DRM, Newton RC (1989) Reversed experimental calibration of the garnet-clinopyroxene
716 Fe-Mg exchange thermometer. Contrib Mineral Petrol 101:87-103
717 Pin C (1990) Variscan oceans: ages, origins and geodynamic implications inferred from
718 geochemical and radiometric data. Tectonophysics 177(1-3):215- 227
719 Pitra P, Ballèvre M, Ruffet G (2010) Inverted metamorphic field gradient towards a Variscan suture
720 zone (Champtoceaux Complex, Armorican Massif, France). J metam Geol 28:183–208

721 Powell R (1985) Regression diagnostics and robust regression in geothermometer/geobarometer
722 calibration: the garnet-clinopyroxene geothermometer revisited. J metam Geol 3:231–243
723 Ribeiro A, Munhá J, Dias R, Mateus A, Pereira E, Ribeiro L, Fonseca P, Araújo A, Oliveira T,
724 Romão J, Chaminé H, Coke C, Pedro J (2007) Geodynamic evolution of the SW Europe
725 Variscides. Tectonics 26:1-24
726 Ricci CA, Carosi R, Di Vincenzo G, Franceschelli M, Palmeri R (2004) Unravelling the tectono-
727 metamorphic evolution of medium-pressure rocks from collision to exhumation of the Variscan
728 basement of NESardinia (Italy): a review. Per Mineral 73:73–83
729 Robardet M (2003) The Armorica "microplate": fact or fiction ? Critical review of the concept and
730 contradictory paleobiogeographical data, Palaeogeogr Palaeoclimatol Palaeoecol 195:125-148
731 Rossi P, Oggiano G, Cocherie A (2009) A restored section of the “southern Variscan realm” across
732 the Corsica-Sardinia microcontinent. C R Geoscience 341:224–238
733 Schulmann K, Konopásek J, Janoušek V, Lexa O, Lardeaux J-M, Edel J-B, Štípská P, Ulrich S
734 (2009) An Andean type Palaeozoic convergence in the Bohemian Massif. C R Geoscience 341:
735 266-286
736 Schulmann K, Kröner A, Hegner E, Wendt I, Konopásek J, Lexa O, Štípská P (2005) Chronological
737 constraints on the pre-orogenic history, burial and exhumation of deep-seated rocks along the
738 eastern margin of the Variscan orogen, Bohemian Massif, Czech Republic. Am J Sci 305:407–
739 448
740 Štípská P, Schulmann K, Kroener A (2004) Vertical extrusion and middle crustal spreading of
741 omphacite granulite: a model of syn-convergent exhumation (Bohemian Massif, Czech
742 Republic). J metam Geol 22:179–198
743 Štípská P, Pitra P, Powell R (2006) Separate or shared metamorphic histories of eclogites and
744 surrounding rocks? An example from the Bohemian Massif. J metam Geol 24:219–240

745 Štípská P, Schulmann K, Powell R (2008) Contrasting metamorphic histories of lenses of high
746 pressure rocks and host migmatites with a flat orogenic fabric (Bohemian Massif, Czech
747 Republic): a result of tectonic mixing within horizontal crustal flow? J metam Geol 26:623–646
748 Tait JA, Bachtadse V, Franke W, Soffel HC (1997) Geodynamic evolution of the European
749 Variscan fold belt: palaeomagnetic and geological constraints. Geol Rundsch 86:585–598
750 von Raumer JF, Bussy F, Stampfli GM (2009) The Variscan evolution in the External massifs of
751 the Alps and place in their Variscan framework. C R Geoscience 341:239-252
752 von Raumer JF, Stampfli GM (2008) The birth of the Rheic Ocean-Early Palaeozoic subsidence
753 patterns and subsequent tectonic plate scenarios. Tectonophysics 461:9–20
754 von Raumer JF, Janoušek V, Stampfli GM (2012) Durbachites-vaugnerites - A time-marker across
755 the European Variscan basement. Géol France, p. 178–180.
756 Vrabec M, Janák M, Froitzheim F, De Hoog JCM (2012) Phase relations during peak
757 metamorphism and decompression of the UHP kyanite eclogites, Pohorje Mountains (Eastern
758 Alps, Slovenia). Lithos 144–145:40–55

759

760 **Figure captions**

761

762 **Fig.1** Geological sketch map of the Bassa Gallura region, North central Sardinia, modified from
763 Frassi et al. (2009) and Carosi et al. (2012). The insert (upper left) corner shows a simplified
764 tectonic sketch map of the Variscan Sardinian chain. The arrow shows the sample locality. PAL:
765 Posada –Asinara Line.

766

767 **Fig. 2** A) Reddish garnet and green amphibole in a polished hand-specimen of the retrogressed
768 eclogites from the Giuncana area; B) Millimetric poikiloblastic garnets with inclusions of
769 omphacite, epidote, quartz, amphibole, plagioclase, rutile and ilmenite, are surrounded by matrix
770 symplectites; C) Omphacite (Cpx_1), quartz, ilmenite and epidote (Ep_{1b}) + plagioclase (Pl_1)

771 inclusions in a garnet poikiloblast; D) Omphacite (Cpx_1) inclusions in garnet, partially replaced by
772 amphibole (Am_{2a}) + quartz symplectite.
773
774 **Fig. 3** A) Omphacite (Cpx_1) inclusion in garnet, partially replaced by clinopyroxene (Cpx_2) +
775 plagioclase (Pl_{2a})+ amphibole (Am_{2b}) symplectite; B) Biotite (Bt_1) + fine-grained plagioclase (Pl_{2b})
776 symplectite after former phengite; C) Poikiloblastic garnet surrounded by a thin corona of green,
777 Al-rich amphibole (Am_{3b}); D) re-equilibrated corona-type microstructure consisting of amphibole
778 (Am_3) + plagioclase (Pl_3) developed between garnet and the matrix; E) Zoned amphibole crystal
779 growing at the expense of matrix symplectite showing a pale-green core surrounded by a darker
780 green rim; F) Matrix amphibole (Am_3) with a core rich in rutile needles oriented parallel to the
781 amphibole cleavages and a rutile-free rim.
782
783 **Fig. 4** X-Ray concentration maps of calcium (a) and magnesium (b) in a selected garnet crystal
784 from sample FC9 showing a very slight compositional zoning. Color code on the right hand side of
785 the images corresponds to counts per seconds.
786
787 **Fig. 5** A) Classification of Cpx_1 clinopyroxene in the (Wo-En-Fs)-Jd-Ae diagram (Morimoto 1988);
788 B) Classification of Cpx_2 clinopyroxene in the Wo-En –Fs diagram (Morimoto 1988). Some
789 additional pyroxene analyses not reported in Table 1 are also shown.
790
791 **Fig. 6** Ca-amphibole classification after Leake et al. (1997) for amphiboles with $Ca_B \geq 1.50$,
792 $(Na+K)_A < 0.50$, $Ca_A < 0.50$ (A) and for amphiboles with $Ca_B \geq 1.50$, $(Na+K)_A \geq 0.50$, $Ti < 0.50$ (B).
793 All textural types of amphiboles are reported. Some additional amphibole analyses not reported in
794 Table 1 are also shown.
795

796 **Fig.7** Metamorphic evolution of the retrogressed eclogites from Giuncana area as inferred from
797 microstructural relationships. Cpx_1, Am_1, Pl_1 and Ep_1: inclusions in garnet poikiloblasts; Cpx_2:
798 simplectitic clinopyroxene; Am_{2a}: amphibole from the amphibole + quartz symplectite; Am_{2b}, Pl_{2a}:
799 amphibole and plagioclase from the clinopyroxene + plagioclase ± amphibole symplectite; Bt_1,
800 Pl_{2b}: biotite and plagioclase from the biotite + plagioclase symplectite; Am_3: matrix amphibole;
801 Am_{3b}: Al-rich matrix amphibole near to garnet crystals; Pl_3: coronitic plagioclase; Am_4: actinolite;
802 Pl_4, Bt_2, Ep_2: albite, retrograde biotite and epidote from the rock matrix.
803
804 **Fig. 8** A) P–T pseudosection calculated in the 500-950°C, 0.1-2.5 GPa range (NCKFMASH+Ti+O
805 system) for the bulk composition of sample FC9 (Table 2) assuming $a(H_2O)$= 1.0. White, light-,
806 medium-, dark-, and very dark-grey fields are di-, tri-, quadri-, penta-, and hexa-variant fields,
807 respectively; B) X_{Mg} [Mg/(Mg+Fe+Ca)] contour lines for garnet; C) X_{Ca} [Ca/(Mg+Fe+Ca)] contour
808 lines for garnet; D) X_{Na} [Na/(Na+Ca)] contour lines for clinopyroxene. The box area in red
809 constrains the P–T conditions for stage I (HP stage). 1: Cpx Am Pl Grt Bt Ep Qtz Mt Ilm; 2: Cpx
810 Am Pl Grt Bt Ep Ep Qtz Ilm; 3: Cpx Am Pl Grt Bt Ep Qtz Ilm; 4: Cpx Wmca Am Pl Grt Ep Qtz
811 Ilm; 5: Cpx Chl Wmca Am Ep Pa Qtz Ilm; 6: Cpx Wmca Am Grt Ep Ep Pa Qtz Ilm; 7: Cpx Chl
812 Wmca Am Grt Ep Pa Qtz Ilm; 8: Cpx Chl Wmca Am Grt Lws Qtz Rt; 9: Cpx Chl Wmca Am Grt
813 Lws Qtz Ilm. KR, P, PN lines are the Krogh Ravna (2000), Powell (1985) and Pattison and Newton
814 (1989) calibrations of the Grt-Cpx geothermometer, respectively.
815
816 **Fig. 9** P–T pseudosection calculated in the 550-850°C, 0.6-1.9 GPa range (NCFMASH system) for
817 the bulk composition of the effectively reacting symplectite microdomain of sample FC9 (Table 2)
818 assuming $a(H_2O)$= 1.0. White, light-, medium-, and dark-grey fields are di-, tri-, quadri-, and
819 penta-variant fields, respectively. X_{Mg} [Mg/(Mg+Fe)] contour lines for clinopyroxene, X_{Na}
820 [Na/(Na+Ca)] for plagioclase and Si content (a.p.f.u.) contour lines for amphibole are also shown.
821 The box area in orange constrains the P–T conditions for stage II (symplectite stage). HBr line is

822 the Holland and Blundy (1994) calibration of the Hb-Pl geothermometer (reaction edenite + albite =
823 richterite + anorthite).
824
825 **Fig. 10** A) P–T pseudosection calculated in the 550-850°C, 0.6-1.9 GPa range (NCFMASH
826 system) for the bulk composition of the effectively reacting amphibole corona microdomain of
827 sample FC9 (Table 2) assuming $a(H_2O)$= 1.0. White, light-, and dark-grey fields are di-, tri-, and
828 quadri-, variant fields, respectively. Contour lines of Si content (a.p.f.u.) in amphibole and X_{Na}
829 [Na/(Na+Ca)] contour lines for plagioclase are also shown. The purple box area constrains the P–T
830 conditions for stage III (amphibole corona stage). HBt and HBr lines are the Holland and Blundy
831 (1994) calibrations for the reactions edenite + 4 quartz = tremolite + albite and edenite + albite =
832 richterite + anorthite of the Hb-Pl geothermometer, respectively.
833
834 **Fig. 11** Comparison between the P-T path obtained for the retrogressed eclogites from Giuncana
835 area with those obtained for other Sardinian eclogites (Cruciani et al. 2012; granulitized eclogites
836 from Punta de Li Tulchi, P-T path 1; Giacomini et al. 2005a; retrogressed eclogites from Golfo
837 Aranci, P–T path 2; Cruciani et al. 2011: Punta Orvili metabasite, P–T path 3). Metamorphic facies
838 modified from Liou et al. (1998).
839
840 **Fig. 12** Simplified tectonic model explaining the possible englobement of the Sardinian eclogites in
841 the framework of the Southern Variscan Realm from Rossi et al., (2009, modified): a) formation
842 of MORB-type eclogite protolith in a small back-arc extensional basin; b) subduction of the North
843 Gondwana margin beneath the Armorica Terrane Assemblage (ATA); c) Early Carboniferous
844 collisional stage. Slab break-off (?). Partially molten orogenic crust hosting granulitized eclogites
845 (High-Grade Metamorphic Complex) extruded over the Low- to Medium- Grade Metamorphic
846 Complex causing the inversion of metamorphic zonation in the bedrock.
847

848 **Table captions**

849

850 **Table 1** Selected microprobe analyses of garnet, amphibole, plagioclase, clinopyroxene, and biotite
851 from sample FC9.

852

853 **Table 2** Bulk rock composition of sample FC9 determined by XRF (first column), bulk
854 composition of sample FC9 used in P-T pseudosection calculation (second column) and bulk
855 compositions for symplectite and amphibole corona microdomains used in P-T pseudosection
856 calculation (third and fourth columns, respectively).

857

858 **Supplementary material:**

859 **Fig. A1** P–T pseudosection calculated for the bulk composition of sample FC9 in the
860 NCKFMASH+Ti+O system assuming $a(H_2O)= 0.5$. 1: Cpx Am Pl Grt Bt Ep Qtz Mt Ilm; 2: Cpx
861 Am Pl Grt Bt Ep Ep Qtz Ilm; 3: Cpx Am Pl Grt Bt Ep Qtz Ilm; 4: Cpx Wmca Am Pl Grt Ep Qtz
862 Ilm; 5: Cpx Chl Wmca Am Ep Pa Qtz Ilm; 6: Cpx Wmca Am Grt Ep Ep Pa Qtz Ilm; 7: Cpx Chl
863 Wmca Am Grt Ep Pa Qtz Ilm; 8: Cpx Chl Wmca Am Grt Lws Qtz Rt; 9: Opx Cpx Pl Grt Kfs Qtz
864 Mt Ilm; 10: Opx Cpx Pl Grt Bt Qtz Rt Ilm; 11: Opx Cpx Pl Grt Kfs Qtz Rt Ilm; 12: Opx Cpx Pl Grt
865 Kfs Qtz Rt; 13: Cpx Wmca Am Grt Bt Qtz Rt.

866

867 **Fig. A2** P–T pseudosection calculated in the NCFMASH system for the bulk composition of the
868 effectively reacting symplectite microdomain in sample FC9 assuming $a(H_2O)= 0.5$.

869

870 **Fig. A3** A) P–T pseudosection calculated in the NCFMASH system for the bulk composition of
871 the effectively reacting amphibole corona microdomain in sample FC9 assuming $a(H_2O)= 0.5$.

872

873 **Fig. A4** Isomodes representing quartz (A) and garnet (B) abundances (vol.%) for the P–T
874 pseudosection calculated for the bulk composition of the effectively reacting amphibole corona
875 microdomain of sample FC9.
876
877 **Table A1** Matrix of residuals for reactions (1) and (2a).
878

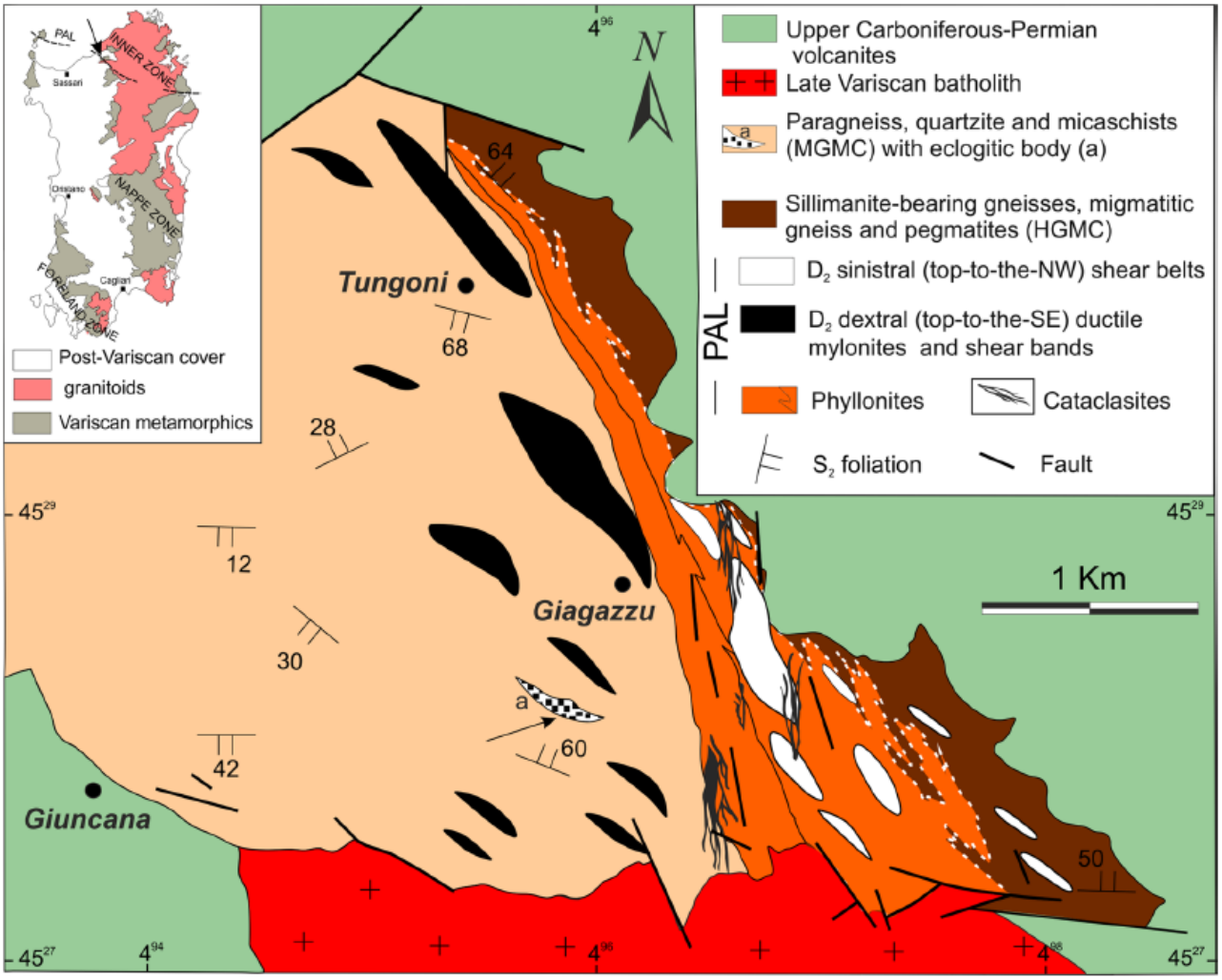

879

880 Fig. 1

881

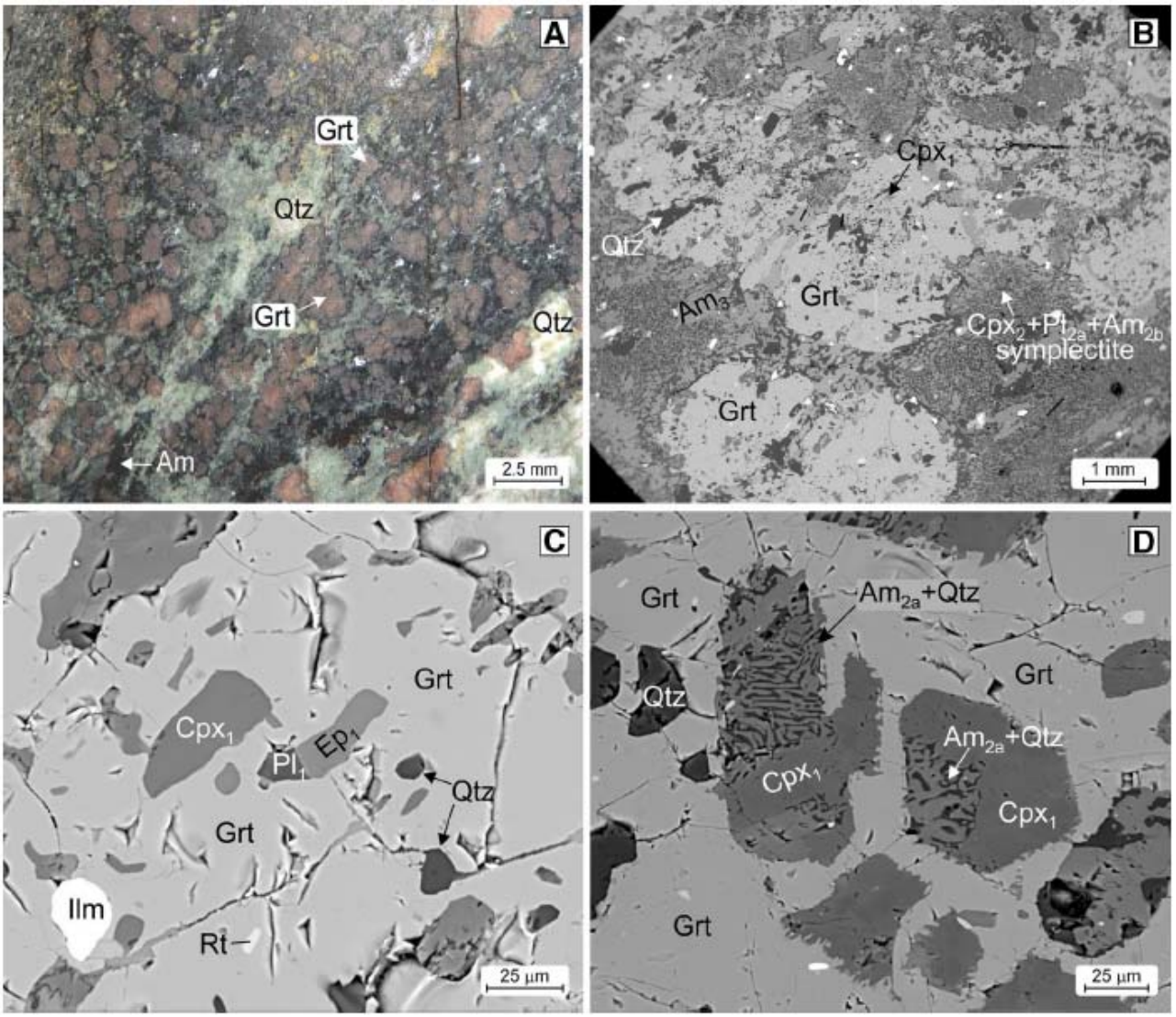

882

883 Fig. 2

884

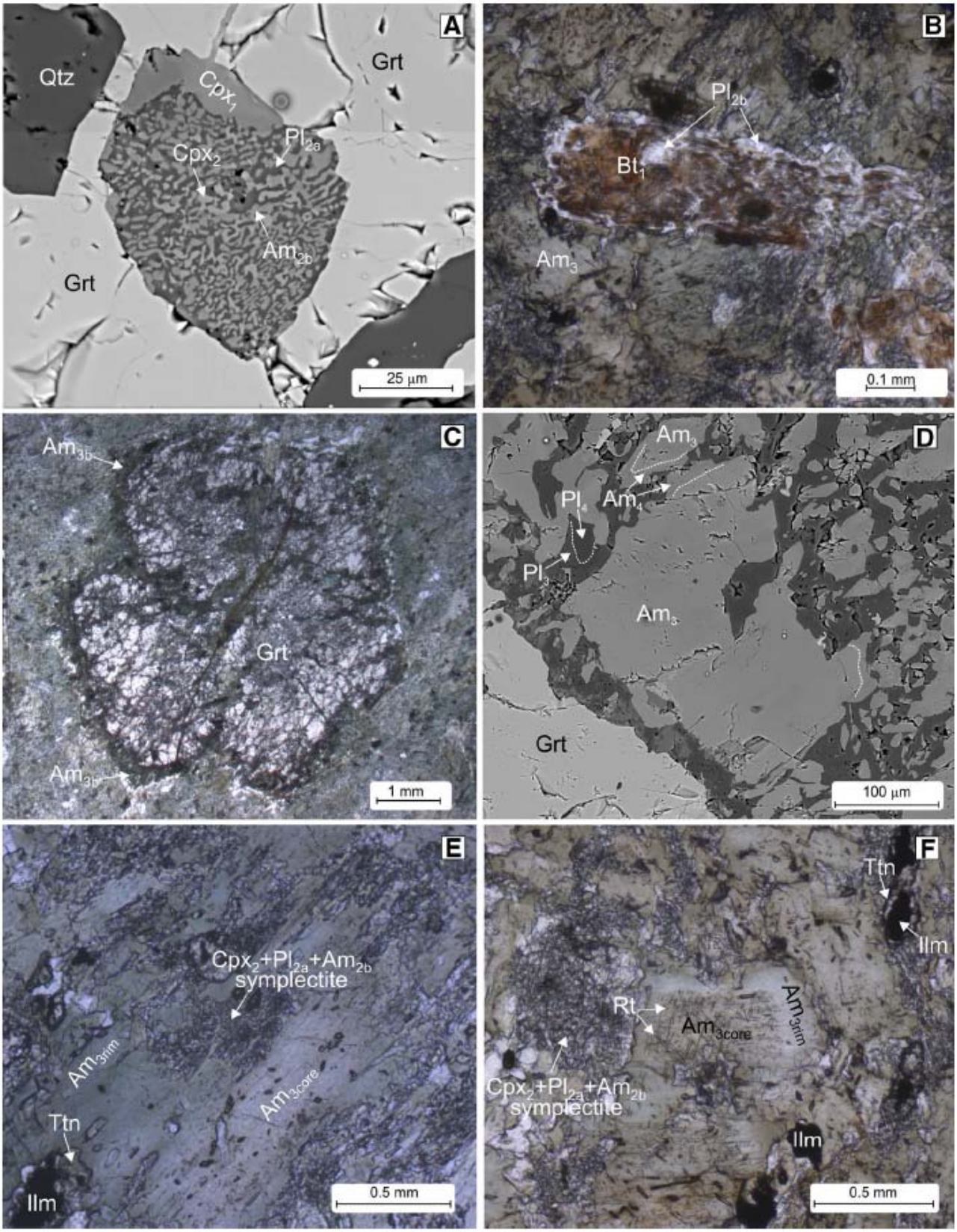
A
Qtz
Cpx1
Grt
Pl2a
Cpx2
Am2b
Grt
25 µm
B
Pl2b
Bt1
Am3
0.1 mm
C
Am3b
Grt
Am3b
1 mm
D
Am3
Pl4
Am1
Pl3
Am3
Grt
100 µm
E
Cpx2+Pl2a+Am2b
symplectite
Am3rim
Am3core
Ttn
Ilm
0.5 mm
F
Ttn
Ilm
Rt
Am3core
Am3rim
Cpx2+Pl2a+Am2b
symplectite
Ilm
0.5 mm

Fig. 3

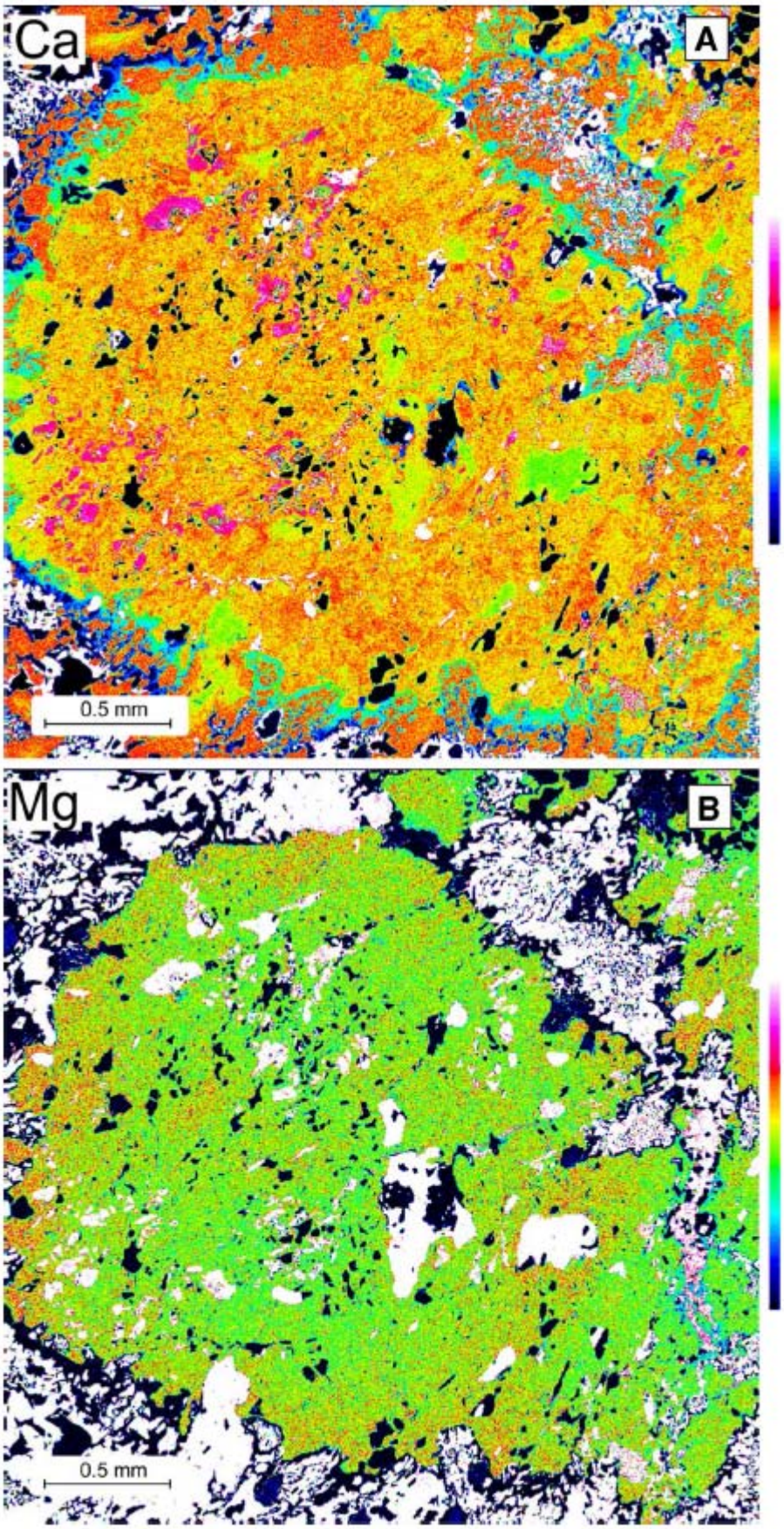

Fig. 4

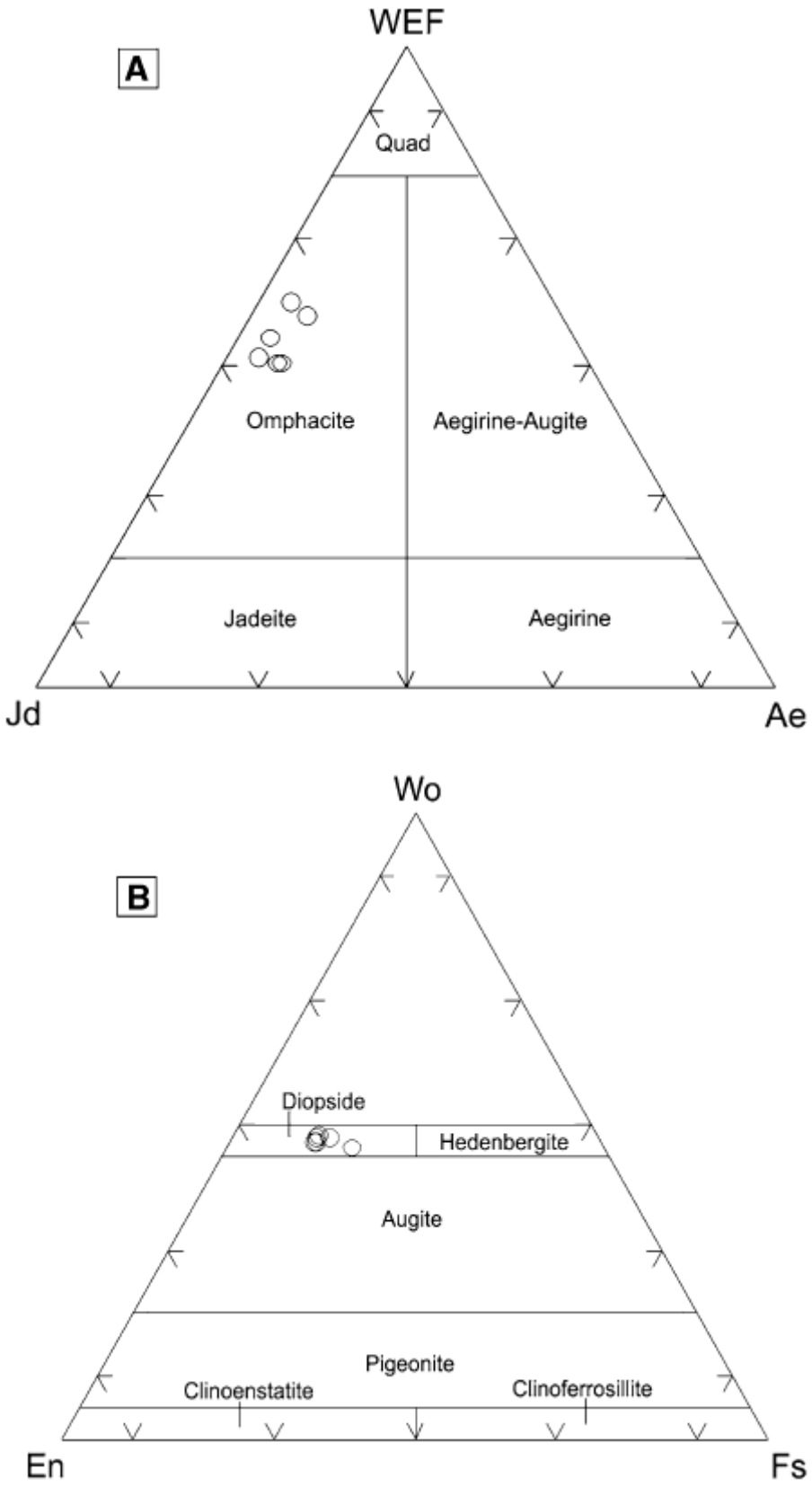

890

891 Fig. 5

892

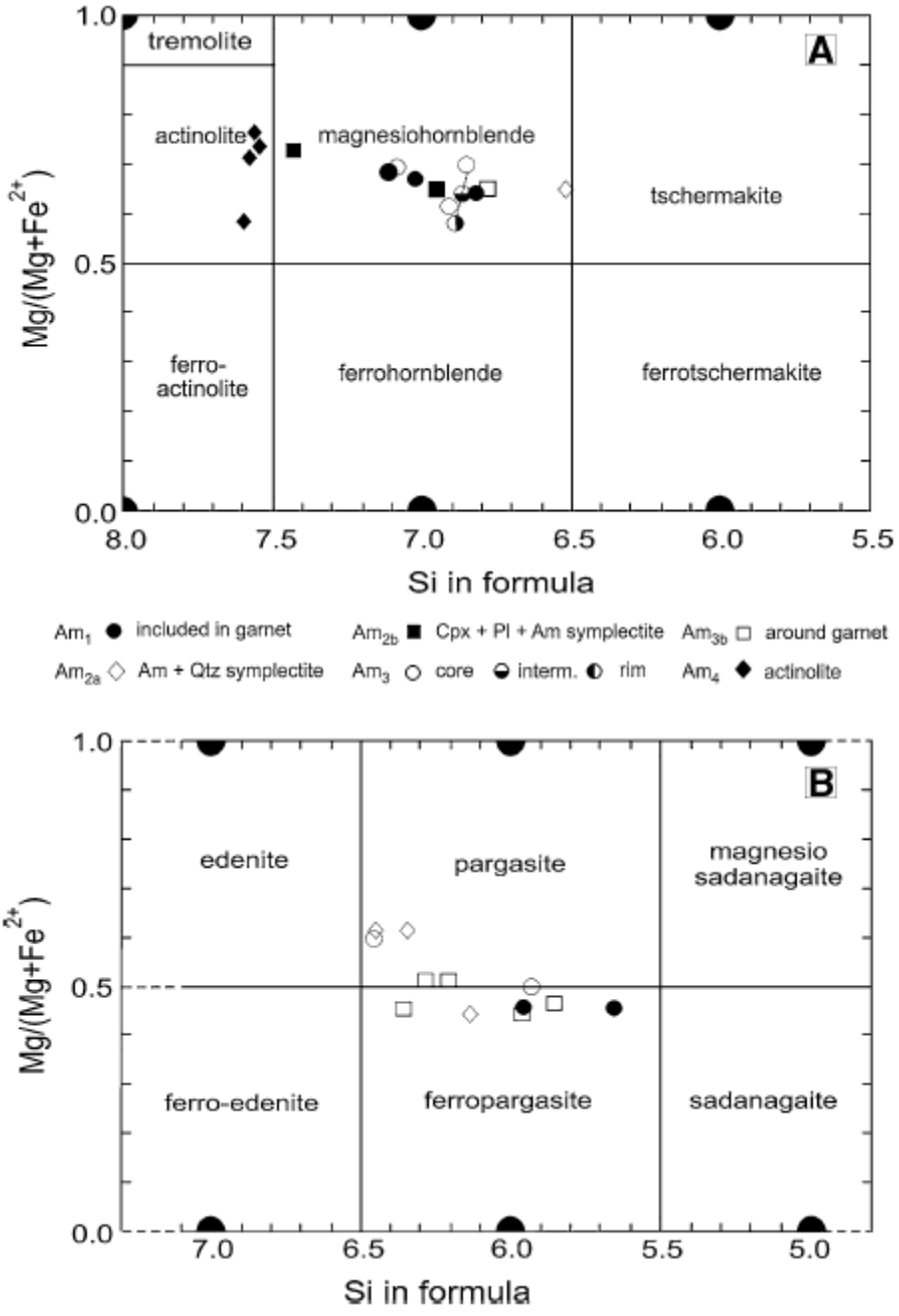

893

894 Fig. 6

895

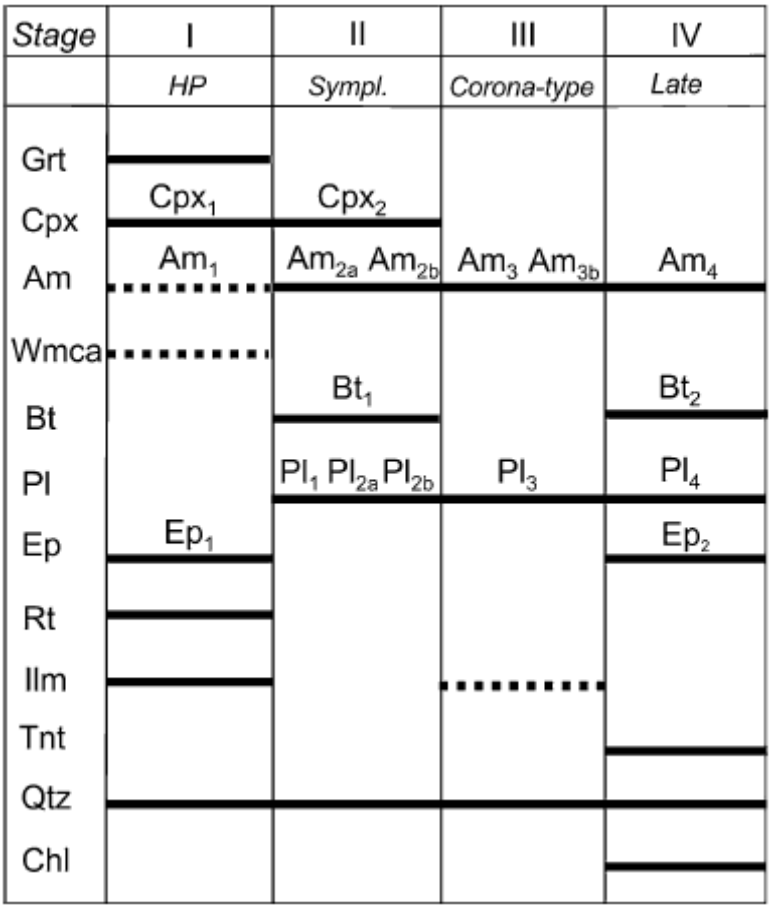
Stage
I
II
III
IV
HP
Sympl.
Corona-type
Late
Grt
Cpx
Am
Wmca
Bt
Pl
Ep
Rt
Ilm
Tnt
Qtz
Chl
Cpx1
Cpx2
Am1
Am2a Am2b
Am3 Am3b
Am4
Bt1
Bt2
Pl1 Pl2a Pl2b
Pl3
Pl4
Ep1
Ep2

Fig. 7

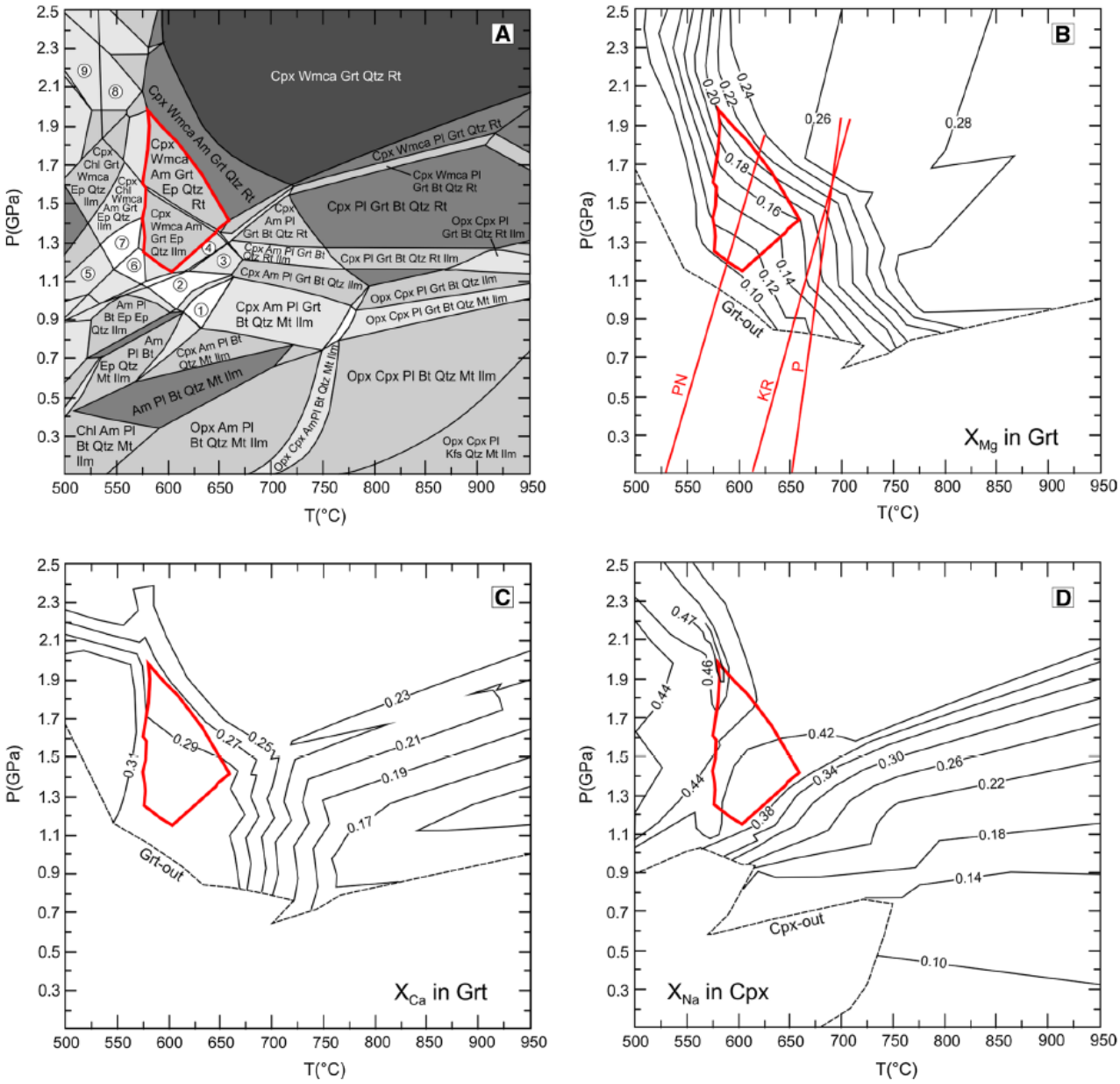

899

900 Fig. 8

901

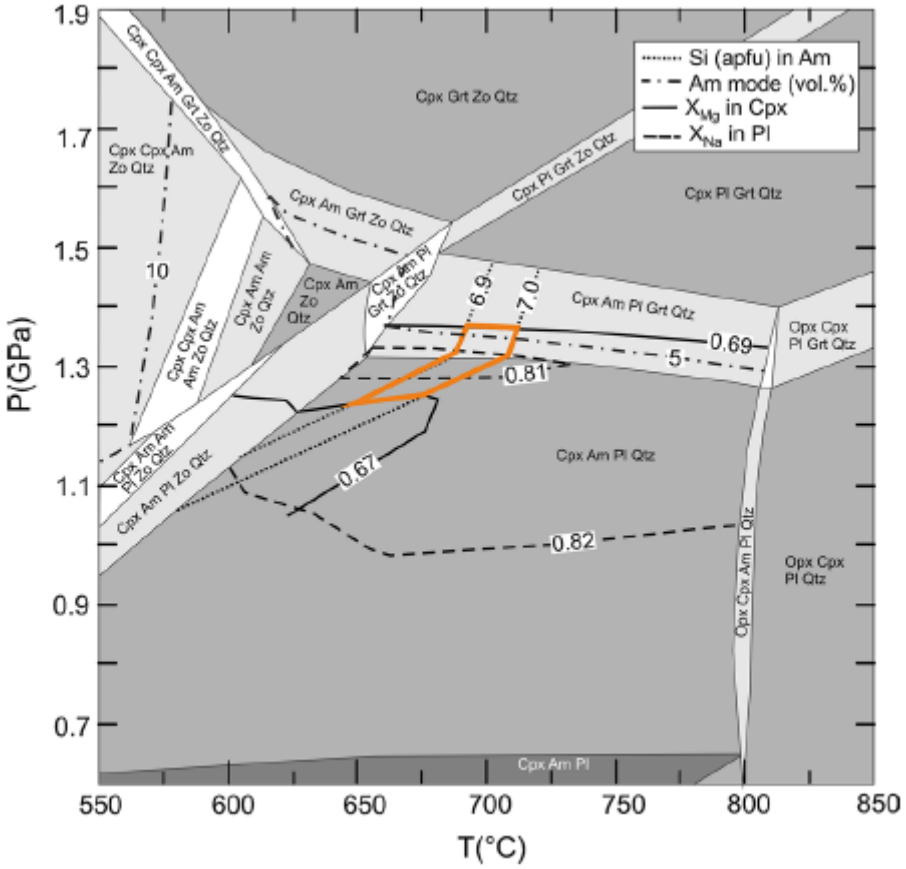

902

903 Fig.9

904

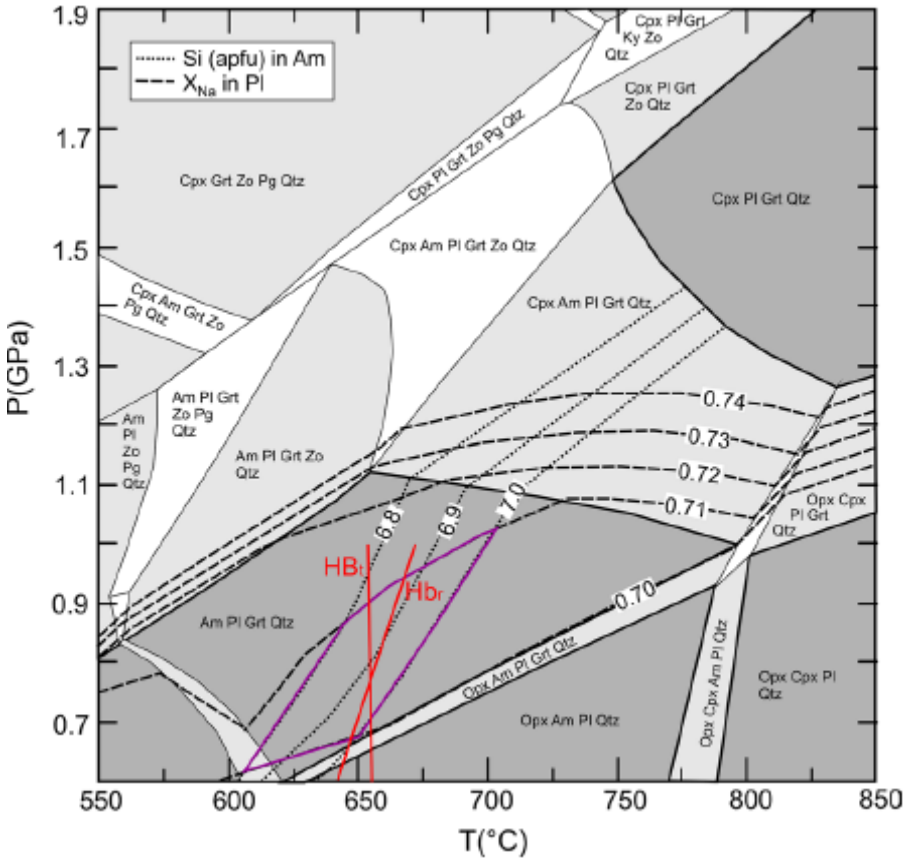

905

906 Fig. 10

907

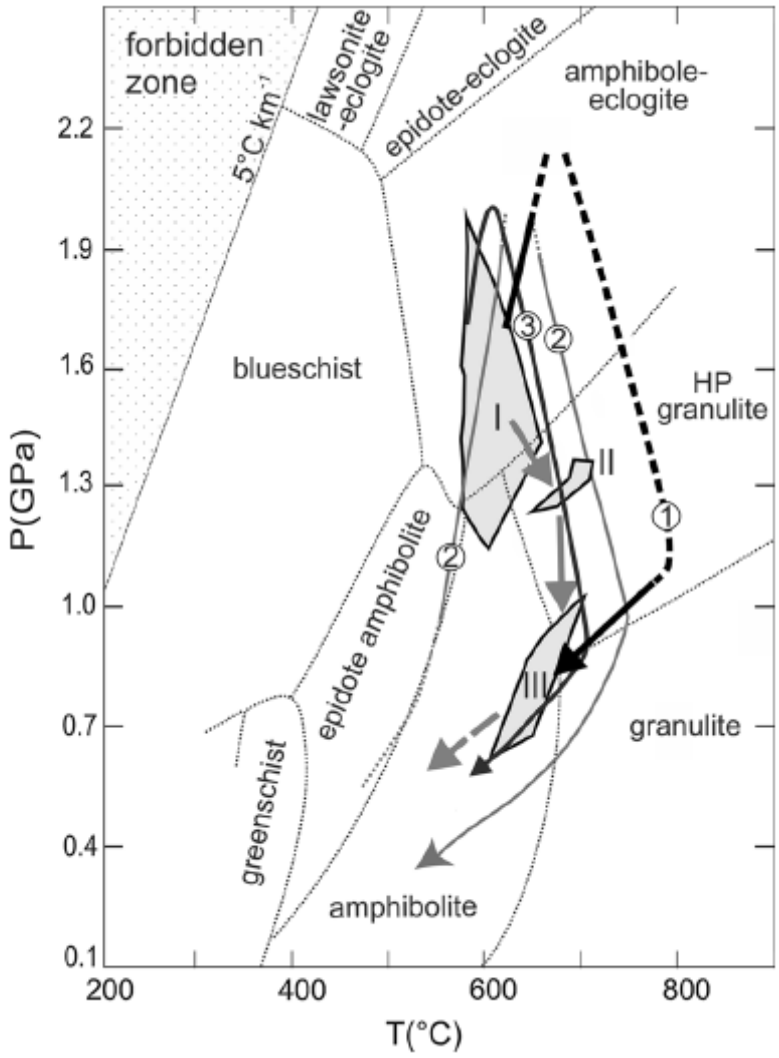

908

909 Fig. 11

910

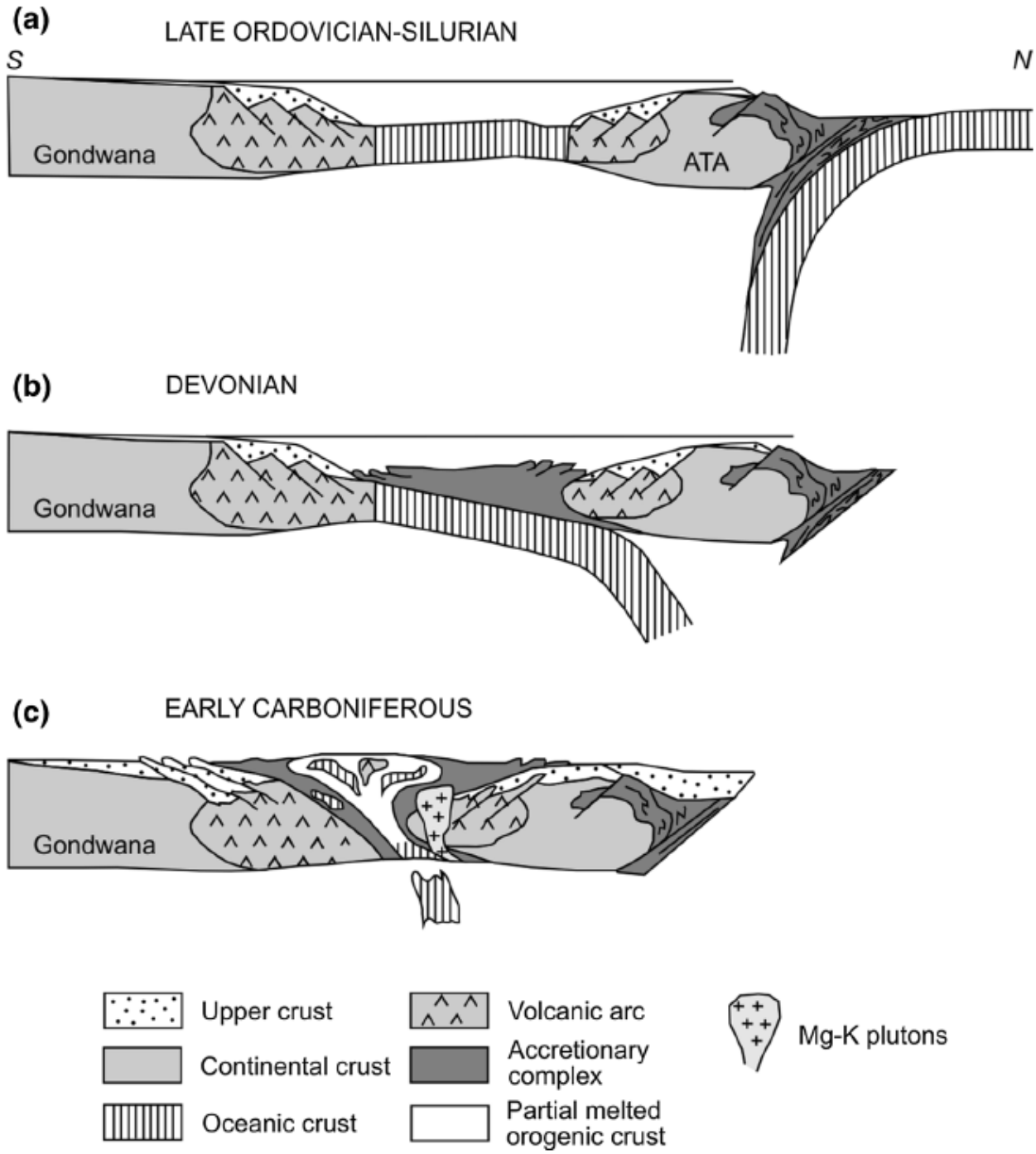

911

912 Fig. 12

913

914

Table 1 Selected microprobe analyses of garnet, amphibole, plagioclase, clinopyroxene and biotite from sample FC9

	Grt core	Grt rim1	Grt rim2	Am1	Am2a	Am2b	Am3core	Am3rim	Am3b	Pl2a	Pl2b	Pl3	Cpx1	Cpx2	Bt1
SiO_2	38.01	38.36	38.19	46.61	40.53	48.30	43.80	46.45	42.47	64.30	57.98	60.95	55.20	53.12	35.93
TiO_2	0.16	0.04	0.16	0.62	0.71	0.84	1.09	0.32	0.92	–	0.01	0.10	0.04	0.04	2.23
Al_2O_3	21.52	21.53	21.46	10.25	14.89	8.67	12.23	9.81	14.47	22.60	25.82	24.81	10.11	1.17	18.41
Cr_2O_3	–	–	0.05	0.07	0.00	0.07	0.08	0.06	0.07	–	–	–	0.04	0.03	0.01
FeO_{tot}	27.01	28.30	27.66	15.45	19.65	14.18	15.59	17.25	17.19	0.06	0.14	0.31	7.91	10.61	18.86
MnO	0.26	0.32	0.22	0.11	0.18	0.12	0.07	0.02	0.07	–	–	–	0.12	0.11	0.13
MgO	3.15	3.20	3.36	11.71	7.54	11.29	10.98	11.00	9.17	0.12	–	–	7.03	12.20	11.38
CaO	10.06	9.61	9.88	10.39	11.28	13.04	11.38	11.26	11.07	4.28	7.48	6.17	13.26	22.22	–
Na_2O	–	–	–	1.47	2.19	1.11	1.85	1.62	2.12	9.39	6.99	7.98	6.47	0.70	0.09
K_2O	–	–	–	0.25	0.78	0.34	0.56	0.17	0.76	0.06	0.09	0.09	0.01	–	9.43
Total	100.17	101.36	100.98	96.94	97.76	97.96	97.63	97.95	98.31	100.81	98.51	100.41	100.19	100.20	96.47
Oxy	12	12	12	23	23	23	23	23	23	8	8	8	6	6	22
Si	2.99	2.99	2.98	6.82	6.13	6.95	6.47	6.83	6.29	2.82	2.63	2.70	1.99	1.99	5.39
Ti	0.01	0.00	0.01	0.07	0.08	0.09	0.12	0.04	0.10	–	0.00	0.00	0.00	0.00	0.25
Al	1.99	1.97	1.97	1.77	2.66	1.47	2.13	1.70	2.52	1.17	1.38	1.29	0.43	0.05	3.25
Cr	–	–		0.01	0.00	0.01	0.01	0.01	0.01	–	–	–	0.00	0.00	0.00
Fe^{2+}	1.77	1.80	1.76	1.44	2.19	1.29	1.64	1.78	1.85	–	–	–	0.24	0.33	2.36
Fe^{3+}	0.01	0.04	0.04	0.45	0.29	0.41	0.28	0.34	0.28	0.00	0.01	0.01	–	–	–
Mn	0.02	0.02	0.02	0.01	0.02	0.02	0.01	0.00	0.01	–	–	–	0.00	0.00	0.02
Mg	0.37	0.37	0.39	2.56	1.70	2.42	2.42	2.41	2.02	0.01	–	–	0.38	0.68	2.54
Ca	0.85	0.80	0.83	1.63	1.83	2.04	1.80	1.77	1.76	0.20	0.36	0.29	0.51	0.89	–
Na	–	–	–	0.42	0.64	0.31	0.53	0.46	0.61	0.80	0.61	0.69	0.45	0.05	0.03
K	–	–	–	0.05	0.15	0.06	0.11	0.03	0.14	0.00	0.01	0.01	0.00	–	1.80
Sum	8.01	7.99	8.00	15.23	15.69	15.07	15.52	15.37	15.59	5.00	5.00	4.99	4.00	3.99	15.64
Alm	0.59	0.60	0.59												
Pyr	0.12	0.12	0.13												
Grs	0.28	0.27	0.28												
Sps	0.01	0.01	0.01												
X_{Mg}				0.64	0.44	0.65	0.60	0.58	0.52				0.61	0.67	0.52
X_{Na}										0.80	0.63	0.70	0.47	0.05	

Table 2 Bulk rock composition of sample FC9 determined by XRF (first column), bulk composition of sample FC9 used in *P–T* pseudosection calculation (second column) and bulk compositions for symplectite and amphibole corona microdomains used in *P–T* pseudosection calculation (third and fourth columns, respectively)

Method	XRF	XRF	Balanced Reaction 1	Balanced Reaction 2a
Microdom.		Whole rock	Symplectite	Amph. corona
Figure		Figure 8	Figure 9	Figure 10
SiO_2	50.72	52.10	58.18	59.47
TiO_2	1.80	1.85	–	–
Al_2O_3	13.15	13.51	11.19	19.98
FeO	–	11.70	5.66	4.56
Fe_2O_3	14.06	1.44	–	–
MnO	0.23	–	–	–
MgO	6.55	6.73	6.50	2.75
CaO	9.79	9.81	13.73	7.14
Na_2O	2.55	2.62	4.74	6.10
K_2O	0.24	0.25	–	–
P_2O_5	0.18	–	–	–
LOI	0.47	–	–	–